Formation and geophysical character of transitional crust at the passive continental margin around Walvis Ridge, Namibia

Gesa Franz[1], Marion Jegen[1], Max Moorkamp[2], Christian Berndt[1], Wolfgang Rabbel[3]

[1]GEOMAR Helmholtz Centre for Ocean Research Kiel

5   [2]Ludwig-Maximilians University of Munich, Germany

[3]Christian-Albrechts University Kiel, Germany

Correspondence to: Gesa Franz (gfranz@geomar.de)

Abstract

When interpreting geophysical models, we need to establish a link between the models' physical parameters and geological

10   units. To define these connections, it is crucial to consider and compare geophysical models with multiple, independent parameters. Particularly in complex geological scenarios, such as the rifted passive margin offshore Namibia, multi-parameter analysis and joint inversion are key techniques for comprehensive geological inferences. The models resulting from joint inversion enable the definition of specific parameter combinations, which can then be ascribed to geological units. Here we perform a user-unbiased clustering analysis of the parameters electrical resistivity and density from two models

15   derived in a joint inversion along the Namibian passive margin. We link the resulting parameter combinations to break-up related lithology, and infer the history of margin formation. This analysis enables us to clearly differentiate two types of sediment cover. Namely, one of near-shore, thick, clastic sediments, and a second one of further offshore located, more biogenic, marine sediments. Furthermore, we clearly identify areas of interlayered massive, and weathered volcanic flows, which are usually only identified in reflection seismic studies as seaward dipping reflectors. Lastly, we find a distinct

20   difference in the signature of the transitional crust south of- and along the supposed hot-spot track Walvis Ridge. We ascribe this contrast to an increase in magmatic activity above the volcanic centre along Walvis Ridge, and potentially a change in melt sources or depth of melting. This characterizes a rift-related southern complex, and a plume-driven Walvis Ridge regime. All of these observations demonstrate the importance of multi-parameter geophysical analysis for large-scale geological interpretations. Furthermore, our results may improve future joint inversions using direct parameter coupling, by

25   providing a guideline for the complex passive margins parameter correlations.

1 Introduction

Passive continental margins can be grouped into "magma-poor" or "non-volcanic", and "magma-dominated" or "volcanic" rifted margins (Blaich et al., 2011; Pérez-Gussinyé & Reston, 2001). The two types feature distinct crustal characteristics, which include extensively rifted continental crust and serpentinized mantle for the magma-poor-, and surface volcanic flows,

30   as well as crustal intrusions for the magma-dominated margin (Blaich et al., 2011; Sawyer et al., 2007). The underlying

reason for the different characteristics is linked to the "Plates vs Plumes" hypotheses, which discusses the triggers of continental break-up in terms of mantle convection, mantle plumes, melt generation, and plate tectonics (Anderson, 2001; Foulger, 2010; Morgan, 1971; Wilson, 1963). The two end-member models ascribe volcanic anomalies and continental rifting to either pure plate tectonic stresses, and upper mantle convection ("plate theory"), or full mantle convection, and

35 deep mantle plumes originating from the core-mantle boundary ("plume theory").

The Walvis Ridge and the Namibian margin have long been a focus of research in terms of passive margin formation and mantle plume-lithosphere interaction. Many regional geophysical studies around Walvis Ridge have investigated typical breakup related geological features such as flood basalts, thickened crust, magmatic underplating, and various crustal

40 intrusions (e.g. Bauer et al., 2003; Fromm et al., 2017a; Gladczenko et al., 1998; Goslin & Sibuet, 1975; Kapinos et al., 2016; Planert et al., 2017; Ryberg et al., 2022), which are reviewed in detail in the next section. While Walvis Ridge is often referred to as a classic plume example (White & McKenzie, 1989), different authors have also argued, that the amounts of magmatism and thermal alteration of the crust at the Namibian coast are too small to justify a continental breakup induced by the arrival of a large plume head (Fromm et al., 2017a; Koopmann et al., 2016; Ryberg et al., 2022).

45

In this study, we complement previous geophysical studies by analysing combined parameter models of electrical resistivity and density. The models, which form the basis for this study, are published in Franz et al. (2021), where data, model resolution, and inversion scheme are presented in detail. Here, we focus on a clustering analysis of the relationship of density and electrical resistivity from two models derived in a cross-gradient coupled joint inversion. By comparing the defined

50 clusters with independent geophysical models and logging data from marine boreholes, as well as reconstructing the temporal margin evolution, we link the clusters to geological units and margin formation stages. This approach complements existing research concerning the breakup mechanisms of the South Atlantic, because the integration of the two parameters electrical resistivity and density improves definition of geological units, and thus advances the interpretation of typical breakup related lithology. Additionally, the characterization of clusters in the electrical resistivity – density correlation, can

55 be a guideline for future improvement of joint inversion using direct parameter coupling (Moorkamp et al., 2017).

2 Geological Setting: Phases of the geodynamic evolution of the Namibian passive continental margin

The late Triassic breakup of the mega-continent Pangea comprises the separation between Gondwana and Laurentia and the rupture of Gondwana in a western (Africa and South America) and eastern (Australia, Antarctica, Madagascar, and India) block (Moulin et al., 2010; Seton et al., 2012).

60

Continental rifting of western Gondwana started in the south in the latest Jurassic (~145 Ma) and propagated northwards until it reached the area around present-day northern Namibia at around 133 Ma (Heine et al., 2013; Macdonald et al., 2003;

Nürnberg & Müller, 1991; Torsvik et al., 2009). Rupture was likely halted at structures such as the Falkland-Agulhas- and Florianopolis fracture zones leading to a segmented rift propagation (Franke et al., 2007; Jackson et al., 2000; Koopmann et

65 al., 2014). The northward propagation of the continental breakup strongly correlates with different phases of the margin evolution, which is outlined in the following sections.

2.1 Phase 1: Early continental rifting

The crust created by the initial northward propagation of continental rifting is characterized by its original background rock,

70 an abundance of different sized fractures and faults, and aligned rift valleys or (half-)graben structures (Clemson et al., 1997; Glen et al., 1997). The West-African background rock is built up from the Precambrian Congo Craton, as well as the Pan-African Kaoko- and Damara fold belts (Begg et al., 2009; Frimmel, 2009; Haas et al., 2021, see Fig. 1). Re-activated faults in these fold belts also pose the main extensional centres of the Jurassic rift stage. They trend north-south in the Kaoko belt and southwest-northeast in the Damara belt (Clemson et al., 1997; Passchier et al., 2002; Salomon et al., 2017). This

75 alignment of Cretaceous rift valleys with the Pan-African fold belts emphasizes the importance of pre-rift basement tectonics on the Cretaeous rift geometry (Gassmöller et al., 2016).

The amount of influence of the Tristan mantle plume in the initiation of continental rifting is still a matter of debate. However, there is evidence that rifting took part prior to magmatic activity (Glen et al., 1997), and that this initial magmatic

80 activity (continental flood basalts) are mainly of upper mantle composition instead of a deep mantle plume source (Franke, 2013; Peate, 1997). Both point to the possibility that the Tristan plume is a consequence of rifting and emanated due to the weakened rifted crust (Franke, 2013). Burke & Dewey (1972) initially described the interaction of mantle plumes and triple junctions. Their theories pose a possible explanation for the maturation of the Tristan plume at its proposed location, through formation of a rifted triple junction along the weak zones of the re-activated faults of the Kaoko-, Damara-, and Gariep fold

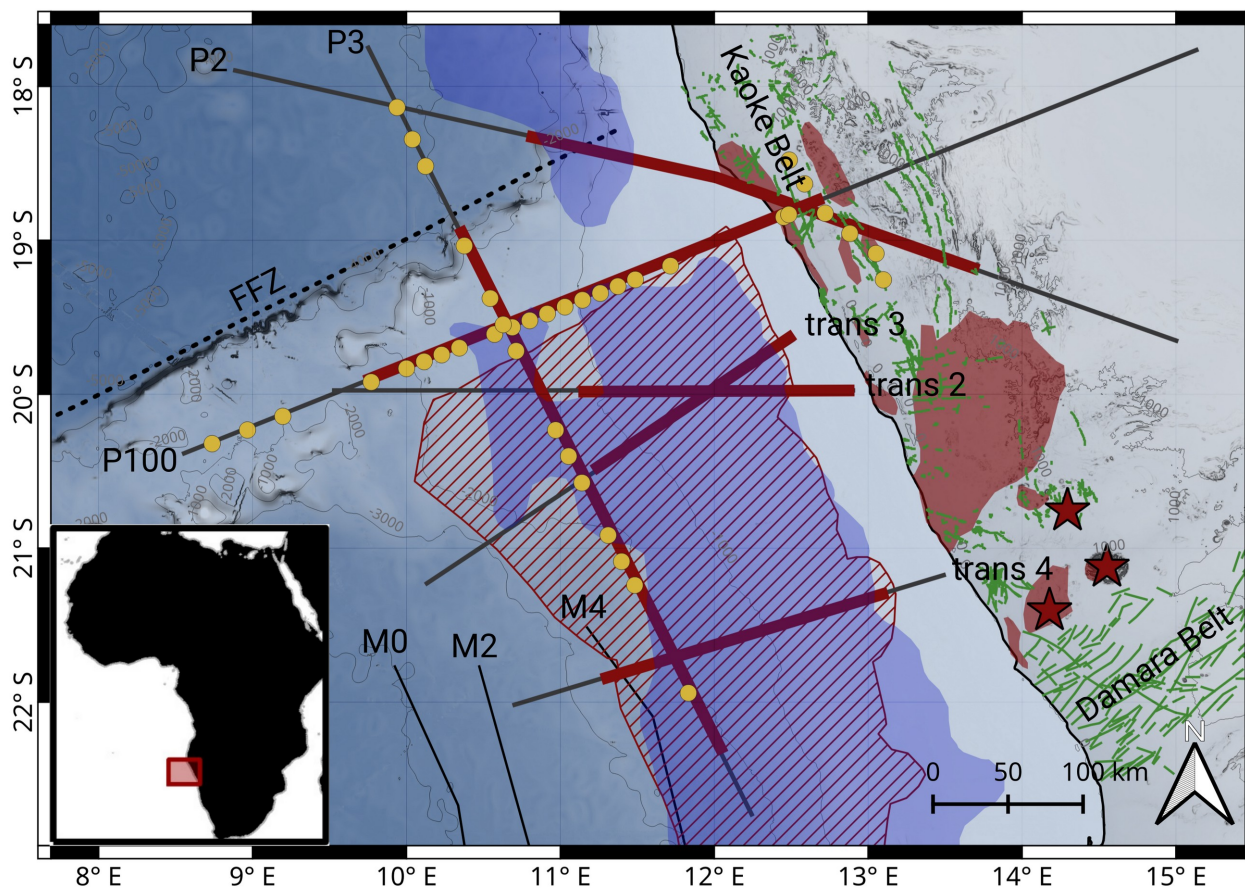85 belts (Franke, 2013; Trumbull et al., 2004).

Figure 1: Topographic map of the survey area with geophysical stations and profiles, as well as geological-, and tectonic features. Yellow circles are marine MT stations, grey lines are seismic profiles, where red marks areas of interpreted high velocity magmatic underplating. Studies are performed by Fromm et al. (2017a, 2015) (profiles P100 and P2), Planert et al. (2017) (profile P3), and Gladczenko et al. (1998). (profiles trans 2 – trans 4). Red dashed area is the outline of seismically imaged seaward dipping reflections (SDR) (Koopmann et al., 2016), black dashed line is the Florianopolis fracture zone (FFZ). Blue area marks the outline of sediment cover thicker than 3 km, taken from Maystrenko et al. (2013). Red areas onshore are the Etendeka continental flood basalts, red stars mark the Brandberg, Messum, and Doros intrusive complexes (Owen-Smith et al., 2017; Teklay et al., 2020). Green lines represent magmatic dykes of the Kaoko and Damara belts (Salomon et al., 2017; Trumbull et al., 2004; respectively). Magnetic lineations M0 to M4 are taken from Moulin et al. (2010).

2.2 Phase 2: Arrival of magmatism

In the continental areas of Namibia, an abundance of intrusive and extrusive structures exhibit the pre-breakup arrival of
100   magmatism. Fracturing and thinning of the rifted crust eventually leads to decompression melting and rise of magma, which
forms three different kinds of features: a) intrusive magmatic bodies, b) magmatic dykes and sills, and c) continental flood
basalts (CFB).

On the Namibian margin, examples for the first (a) are the Jungfrau- and Sargdeckel-, Messum-, Brandberg-, and Doros
105   complexes located in the most southern part of the exposed Etendeka magmatic province (Teklay et al., 2020; Harris et al.,
1999; Schmitt et al., 2000; Owen-Smith et al., 2017; respectively, see Fig. 1). All of them are intrusive, igneous rocks of
mixed composition, including depleted, shallow mantle as well as enriched, deeper, plume-like components, indicating
interaction of the Tristan mantle plume with the overlying lithosphere. Despite their varying chemical composition, they are
all massive magmatic bodies, which were trapped in the crust and have now emerged to the surface.

110

Melts, that were not trapped in the described massive intrusive bodies, may rise to the surface as magmatic dykes (b).
Examples on the Namibian margin are the Huab-, and Henties Bay-Outjo dyke swarms, as well as dykes oriented along the
Kaoko Belt (Duncan et al., 1989; Keiding et al., 2013; Trumbull et al., 2004; Salomon et al., 2017; respectively). The
orientation of these dykes correlates with the faults and fractures described in Sect. 2.1, thus, melts ascended in the pathways
115   created by preceding continental rifting and may be accompanied by horizontally emplaced sills.

These magmatic dykes then form the feeding system for the massively extruded continental flood basalts (c) which are
asymmetrically distributed over the African- and South American margin as the Etendeka- and Paraná CFB provinces,
respectively (Peate, 1997). Possible reasons for the asymmetry include the position of the Tristan mantle plume below the
120   Paraná province (O'Connor & Duncan, 1990), an uneven lithosphere base (Gassmöller et al., 2016; Thompson & Gibson,
1991), pronounced topography on the African side through uplift hindering eastward magmatic flow (White & McKenzie,
1989), or a sheared extension leading to a rotation of South America (Aslanian et al., 2009; Peate, 1997)

2.3 Phase 3: Transition from rifting to continental breakup

A clear definition of the transition from rifting to breakup (continent-ocean-transition, COT) is generally difficult. The zone
125   of transitional crust is highly variable, consisting of initially rifted and intruded continental crust described above, followed
by an increase of dykes and horizontal sill intrusions, and eventually magmatic flows on the surface, which may appear
consistently or periodically (e.g. Eldholm et al., 2000). A distinct continent-ocean-boundary (COB) is usually defined by the
onset of submarine spreading, characterized by magnetic linear anomalies and seismic structure (Gladczenko et al., 1998;
Rabinowitz & Labrecque, 1979). At the Namibian margin, the Cretaceous magnetic quiet zone coincides with continental

130 breakup, impeding a clear COB mapping by magnetic lineations (Koopmann et al., 2016; Moulin et al., 2010; Seton et al., 2012). Additionally, different mechanisms for magnetic lineation generation have been described, e.g. a linear pattern masked by overlying subaerial sheet flows, which may challenge this classical definition (Collier et al., 2017).

The increase of magmatic activity leads to an abundance of intrusive igneous material, referred to as magmatic underplating,
135 which is usually associated with high velocity, high density lower crustal bodies (Becker et al., 2014; Fromm et al., 2017a; Gernigon et al., 2004; Hirsch et al., 2009; Mjelde et al., 2007, see Fig. 1). They may be produced by an accumulation of mantle melts below the crust due to a contrast in density, or by massive intrusions into the heated and weakened lower crust (Eldholm et al., 2000; Franke, 2013; White et al., 1987). Continued ascend of increasing amounts of melts eventually leads to surface flows.

140

Typical features associated with these surface flows at the transition from rifting to drifting are immense sequences of seaward dipping reflectors (SDR) in marine seismic studies (Franke, 2013; Mutter et al., 1982; Paton et al., 2017; Planke et al., 2000, see Fig. 1), and a wide, chaotic magnetic anomaly (anomaly G, or LMA for large magnetic anomaly in Rabinowitz & Labrecque, 1979; Moulin et al., 2010, respectively). This anomaly results from the SDR's periodic emplacement and may
145 overlap with the classic COB marked by underlying magnetic lineations (Collier et al., 2017; Paton et al., 2017; Planke et al., 2000). SDR's are defined as series of compact magmatic flows interbedded with sediments, tephra, or hyaloclastites and may be emplaced subaerially or subaqueously in shallow marine environments (Jackson et al., 2000; Planke et al., 2000). The different depositional environments and possibly chemical composition distinguishes them from the initial continental flood basalts.

150 **2.4 Phase 4: Halted breakup at the Florianopolis fracture zone**

The crustal structure of Walvis Ridge changes strikingly rapid at the Florianopolis Fracture Zone (FFZ, also referred to as Rio Grande fracture zone, see Fig. 1) (Goslin & Sibuet, 1975; Planert et al., 2017). While thickened crust and the features described above (magmatic underplating, periodic magmatic flows, and magmatic dykes) characterize the COT zone south of Walvis Ridge, the crust north of the FFZ is distinctly thinner, with little to no magmatic signature (Aslanian et al., 2009;
155 Blaich et al., 2011; Planert et al., 2017).

Continental breakup around Walvis Ridge is dated at ~133 Ma, while breakup north of the FFZ took place at around 112 Ma, leading to ~20 Ma halted spreading (Heine et al., 2013; Moulin et al., 2010). A likely reason for this pause is a change in plate motion around this time, from a west-east, to a southwest-northeast extension. Most likely, the halted breakup plays an
160 important role in the formation of an abundance of adjacent magmatic features like the thickened crust below Walvis Ridge and massive packages of interbedded flows (SDR) (Bauer & Schulze, 1996; Fromm et al., 2017a; Gladczenko et al., 1998).

These pronounces structures caused by a prolonged plume-ridge interaction may have created a structural boundary preventing northward horizontal flow of the rising plume material (Georgen & Lin, 2001; Planert et al., 2017).

2.5 Phase 5: Ridge jump and continued continental breakup

165 The maximum melt production around Walvis Ridge is dated at ~122 Ma, indicating the arrival of the plume tail at the base of the lithosphere and subsequent decrease of magmatism (Gassmöller et al., 2016). Then, an eastward ridge-jump moved the centre of breakup directly adjacent to the Angolan coast (~112 Ma), which lead to an abrupt transition between continental and oceanic crust (Aslanian et al., 2009; Moulin et al., 2010). The delayed breakup lead to considerably more continental rifting (width of ~350 km) north of the FFZ compared to the maximum of ~100 km south of the boundary

170 (Torsvik et al., 2009). While the crust north of the FFZ is largely unaffected by the plume material (Gassmöller et al., 2016), Aptian salt basins further north are evidence for a preceding, syn-rift shallow marine environment (Blaich et al., 2011; Heine et al., 2013; Torsvik et al., 2009). For the preceding reasons, the continental margin north of the FFZ may be referred to as "magma-poor" (Blaich et al., 2011).

3 Method

175 In order to identify specific parameter ranges and -relationships representing the different stages of continental breakup at the Namibian margin, we analyse electrical resistivity and density models which have been derived from a joint data inversion with cross-gradient coupling, based on marine magnetotelluric- (MT) and satellite gravity data, respectively (Franz et al., 2021). Marine MT stations were deployed along two perpendicular profiles along- (profile P100) and across (profile P3) Walvis Ridge, with a stations spacing of ~10 km (Fig. 1). Gaps in the final station distribution result from a loss of data

180 or insufficient data quality. The data set is expanded onshore by eight land MT stations from the survey presented in Kapinos et al. (2016). Electrical resistivity and density are sensitive to changes in fluid content (including melt and water), rock density or porosity, as well as rock composition (Bedrosian, 2007; Hinze et al., 2013; Moorkamp, 2022). Therefore, typical breakup related lithologies, such as rifting, magmatic upwelling, and subaerial-, as well as subaquatic phases described in the previous section, should impact the resistivity and density of crustal- and mantle rocks. Since electrical resistivity and

185 density do not necessarily respond likewise to, for example fluid content or geochemical variations, it is reasonable to expect a differentiation of particular resistivity-density pairs identified using a cluster analysis of the congruent resistivity and density models. The determined clusters can then be linked to lithological units and continental break-up stages. We therefore present a clusters analysis along the passive margin around Walvis Ridge. Through a comparison to literature parameter values and geophysical studies, we show that the clusters can indeed distinguish lithologies or rock types linked to

190 the continental breakup stages. The applied data, inversion scheme, sensitivity-, and model analysis of the congruent resistivity and density models are described in much detail in Franz et al. (2021); Jegen et al. (2016); and Moorkamp et al. (2011). GMM and other fuzzy clustering methods have also been used to guide joint inversion schemes by adding

petrophysical data and improving subsequent geological interpretations (e.g. Astic & Oldenburg, 2019; Astic et al., 2020; Lelièvre et al., 2012; Paasche & Tronicke, 2007; and Sun & Li, 2017).

195

The gravity data inversion yields a density anomaly model, defining anomalies from a simple 2-layer reference model containing terrain and Moho topography. We applied the Moho topography correction to account for the strong gravity difference caused by the substantial difference in thickness between the continental- and oceanic crust (cp. Fig. 4 in Franz et al., 2021). Moho depth was derived from a regional density model (Maystrenko et al., 2013) and a global crustal thickness

200 reference (Laske et al., 2013). For consistency, we perform separate cluster analysis for the crustal- and mantle domain according to the applied Moho topography correction. In addition, we isolate a sediment layer for the clustering. We do this, because we observed, that physical parameter clusters show a significant overlap sediment and upper crustal values. The separation improves the differentiation between the shallowest model features and upper crustal components. Identification of sediment thickness is based on two seismic velocity models of Fromm et al. (2017a) and Planert et al. (2017) along profile

205 P100 and P3, respectively. Since they both use velocity modelling and reflection seismic data to define the sediment basement, the sediment thickness is well constrained. The parameter analysis thus focuses on three domains, which are: a) sediment cover, b) crust, c) mantle.

In each of these three domains, we perform clustering using logarithmic electrical resistivity ($\log_{10}(\rho_a)$ in Ωm) with absolute

210 density (d in kg m^{-3}) of the same model cell. Although the inversion is conducted on a 3D model cube and both data sets have 3D sensitivity, previous tests indicate, that the resistivity model's resolution capabilities are limited away from the MT stations (Franz et al., 2021). We therefore use only model cells with a maximum horizontal distance of 10 km to the MT station location (Fig. 1). Absolute density values are simply the sum of the inversion density anomaly model, and the crustal- (2810 kg m^{-3}) or mantle- (3222 kg m^{-3}) density according to whether the model cell belongs to the crustal- or mantle region.

215 The resulting parameter correlations are clustered separately in each of the three domains using the probabilistic Gaussian mixture model (GMM) algorithm (Géron, 2019; McLachlan et al., 2019). GMM generates clusters based on the assumption, that the model is assembled from a mixture of Gaussian distributions and applies fuzzy- or soft clustering. Such a soft assignment allows for an overlap of clusters, and for each data point (resistivity-density pair) the probability, that the data point belongs to any of the clusters, is determined. We chose the GMM approach, because our two coupled models are

220 smoothed independently from another during the inversion, which leads to model areas of less defined parameter correlations in between the major distinct anomalies. Also, in contrast to hard clustering methods, GMM may dampen clusters arising from inversion artefacts. For example, one cluster may summarize a small model artefact by the highest probability, but when analysing the other cluster's probabilities, it may merge with a different, more geologically plausible cluster. In both cases, the analysis of the probabilities of all clusters in soft clustering adds information and therefore benefits

225 cluster interpretation. Each gaussian distribution is defined by it's mean and covariance matrix, where the covariance matrix defines the shape and orientation of the typically ellipsoid clusters (Géron, 2019). We leave the Gaussian mixture's

covariance matrix unconstrained, to avoid a priori limitations of clusters. In order to achieve most stable results, we repeated the optimization process 20 times, at which point we experienced no more variation depending on the initial parameter selection in the soft clustering convergence. Due to the initial random cluster selection of the algorithm, classification of the

230 clusters' edges slightly varies within these replicates. While the clusters' centres are robust, the fuzzy overlaps of adjacent clusters experience small changes in the probability estimate, leading to a different primary cluster assignment. After 20 repetitions, we found that the cluster edges were also robust. The number of clusters in each domain is determined by evaluating the two criteria AIC (Akaike information criteria, Akaike, 1974), and BIC (Bayesian information criteria, Schwarz, 1978), which are theoretical information criteria optimizing data fit (maximum likelihood), while minimizing the

235 number of defined clusters. With both methods, we use the elbow method to determine the minimum AIC/BIC value with a reasonably small number of clusters. We chose two sediment domain clusters, and each four in the crustal- and mantle domains, respectively (Fig. 2). By correlating the identified clusters with the spatial location along the MT station's profiles, we are able to link them to the geodynamic breakup phases described in the previous section.
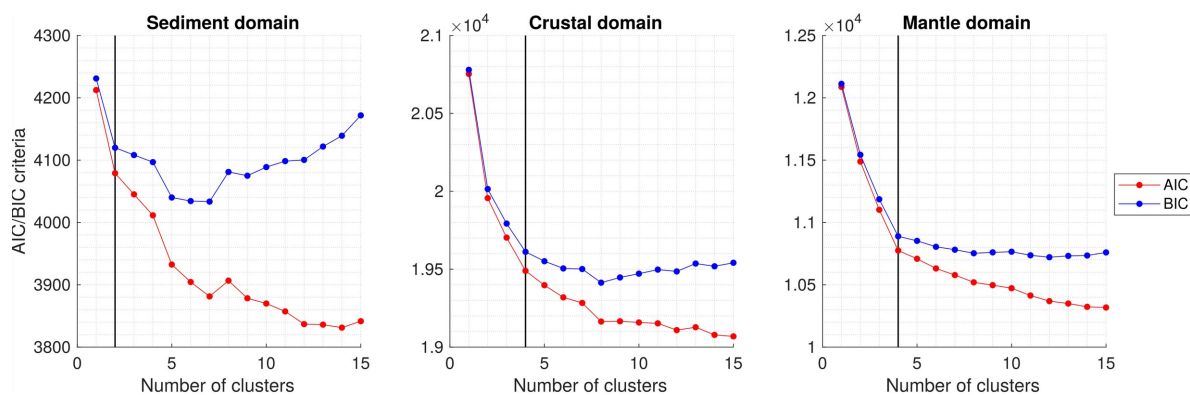

240 **Figure 2: Theoretical information criteria AIC (Akaike information criteria) and BIC (Bayesian information criteria) to determine the number of clusters in each of the three domains. The vertical black line marks the chosen number of clusters, which is two in the sediment domain, and four in the crustal- and mantle domain, respectively.**

9

4 Results: Identified clusters of characteristic physical parameter values and -relationships and their spatial correlation

245

Here we describe the electrical resistivity and density clusters for the sediment-, crustal-, and mantle domain and their location within the models along the Namibian margin.
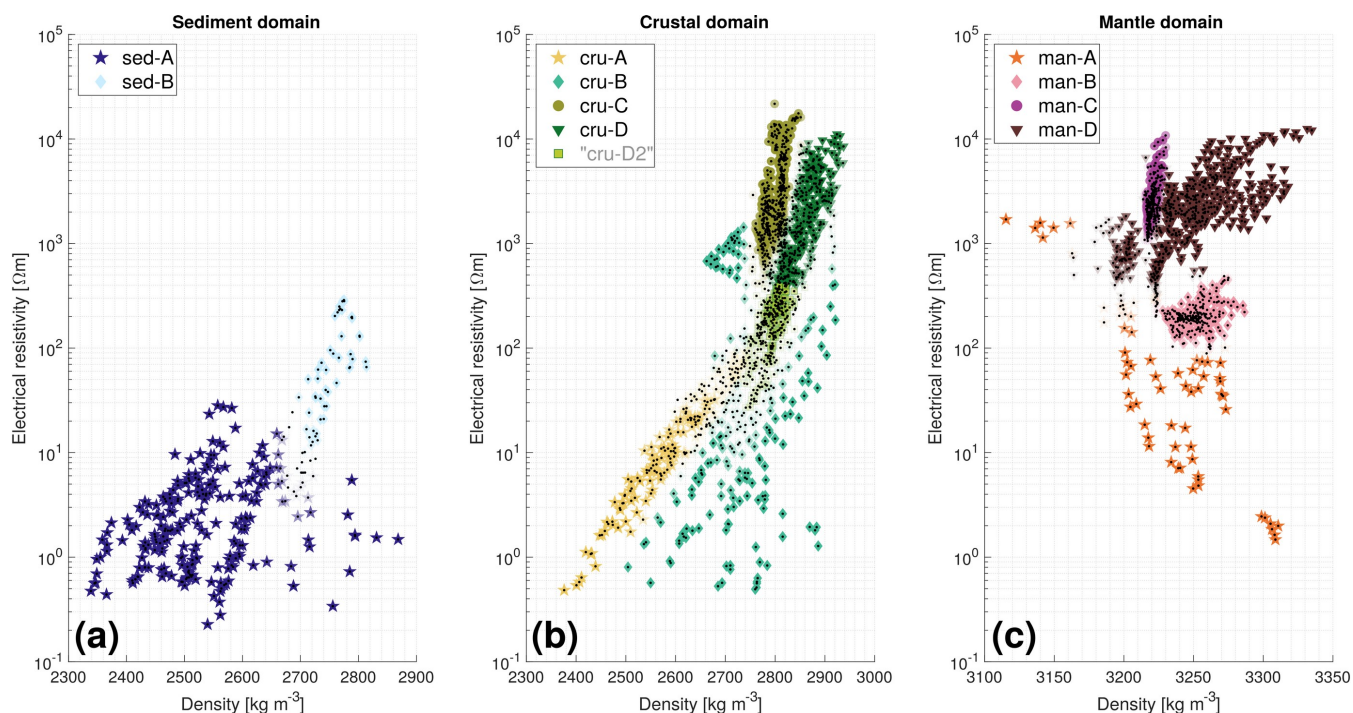
Figure 3: Cross-plots of electrical resistivity and density and their identified clusters. Colour saturation of symbols is proportional to posterior probability within Gaussian mixture model. Less saturated symbols depict decreased certainty of the cluster classification. (a): Sediment domain (depth extent defined by seismic models of Fromm et al. (2017a) and Planert et al. (2017)). (b): Crustal domain (depth extent defined as sediment basement to Moho derived from Laske et al. (2013) and Maystrenko et al. (2013)). Cluster "cru-D2" is manually defined by dividing the identified cluster cru-D horizontally at 400 Ωm. (c): Mantle domain (below Moho).

4.1 Sediment domain

255

Clustering of electrical resistivity and density of the sediment domain (as defined by sediment thicknesses retrieved from Fromm et al. (2017a) and Planert et al. (2017)), results in two clusters with the following characteristics and spatial distribution:

260 Cluster sed-A (indigo stars in Fig. 3a) comprises low density values (mostly < 2700 kg m⁻³), and low resistivity values (<30 Ωm). The model cells belonging to this cluster are mainly situated in the eastern part of profile P100 (stations MT25 –

MT34, Fig. 4) and the central and southern part of profile P3 (MT6 – MT23, Fig. 5). The associated cells cover the entire sediment layer, which in most of these regions has a thickness between 1 and 3 km.
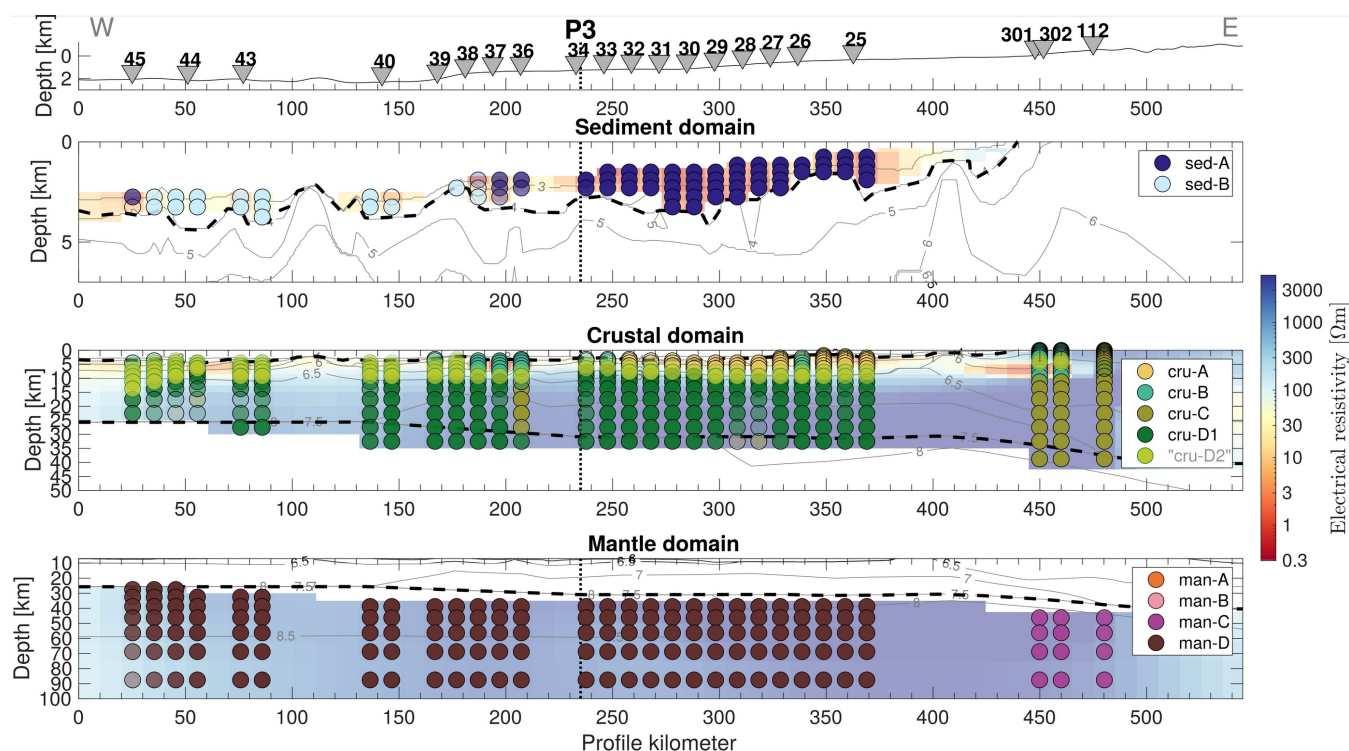
Figure 4: Vertical section along profile P100 through the 3D electrical resistivity model overlaid with parameter clusters. Top panel shows topography, location of MT stations, and intersection with profile P3. Second panel: Results for sediment domain. Third panel: Results for crustal domain. Fourth panel: Results for mantle domain. Thin lines are seismic velocity contours, thick dashed lines are sediment basement and Moho, (from Fromm et al., 2017a). Vertical dotted line denotes intersection with profile P3. Colour saturation of circles is proportional to posterior probability of the Gaussian mixture model. Less saturated circles depict decreased certainty of the cluster classification.

The second cluster sed-B (cyan diamonds in Fig. 3a) comprises slightly higher densities (> 2700 kg m^{-3}) and electrical resistivities (> 10 Ωm, up to ~300 Ωm). The presence of atypical high electrical resistivity values in the sediment cluster B points to a possible problem with the definition of the sediment domain (see Sect. 3). The sediment thicknesses used to define the sediment domain are from independent seismic velocity models, and may not always exactly coincide with the joint electrical resistivity/density models. However, this may also be due to a vertical model cell size at this depth of mostly 1 km, which is too large to sufficiently parameterize accurate sediment thicknesses and therefore leads to a mixed influence of sediments and crust in model cells at the base of the sediment domain. Nevertheless, our investigations have indicated a lithological difference of the two sediment clusters, which will be further discussed in the next section. In the parameter models, the cells of cluster sed-B are localized further west along profile P100 (stations MT38 – MT45, Fig. 4), and north of

Walvis Ridge on profile P3 (stations MT1 and MT2, Fig. 5). Just as we've seen for cluster sed-A, the cells cover the entire sediment domain layer with thicknesses mostly between 1 and 2 km.

Magnetotelluric data resolves, particularly for shallow anomalies, only the conductivity-thickness product, i.e. electrical conductance (Parker, 1980). To address this ambiguity, we calculate the conductance of each cluster associated with a conductive anomaly (sed-A, sed-B, and cru-A) underneath each marine MT station, by multiplying the sum of the cluster's vertically stacked cells' thickness, with the stacked cells' mean electrical conductivity. The clusters sed-A and sed-B are clearly separated by their conductance values: sed-A yields values between ~100 and ~5000 S while conductance values of sed-B are much lower with a range between ~40 and ~100 S (Fig. 6).
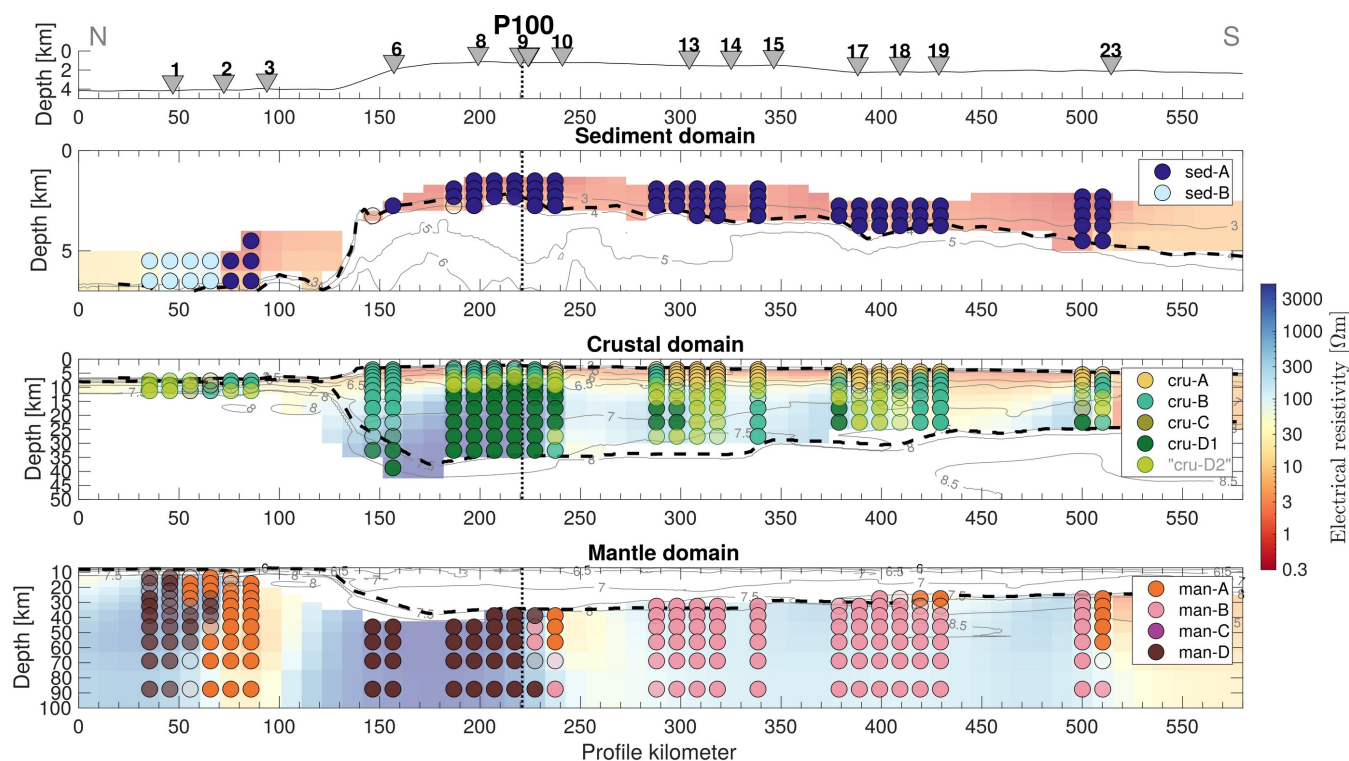

Figure 5: Vertical section along profile P3 through the 3D electrical resistivity model overlaid with parameter clusters. Top panel shows topography, location of MT stations, and intersection with profile P100. Second panel: Results for sediment domain. Third panel: Results for crustal domain. Fourth panel: Results for mantle domain. Thin lines are seismic velocity contours, thick dashed lines are sediment basement and Moho, (from Planert et al., 2017). Vertical dotted line denotes the intersection with profile P100. Colour saturation of circles is proportional to posterior probability of the Gaussian mixture model. Lighter saturated circles depict decreased certainty of the cluster classification.
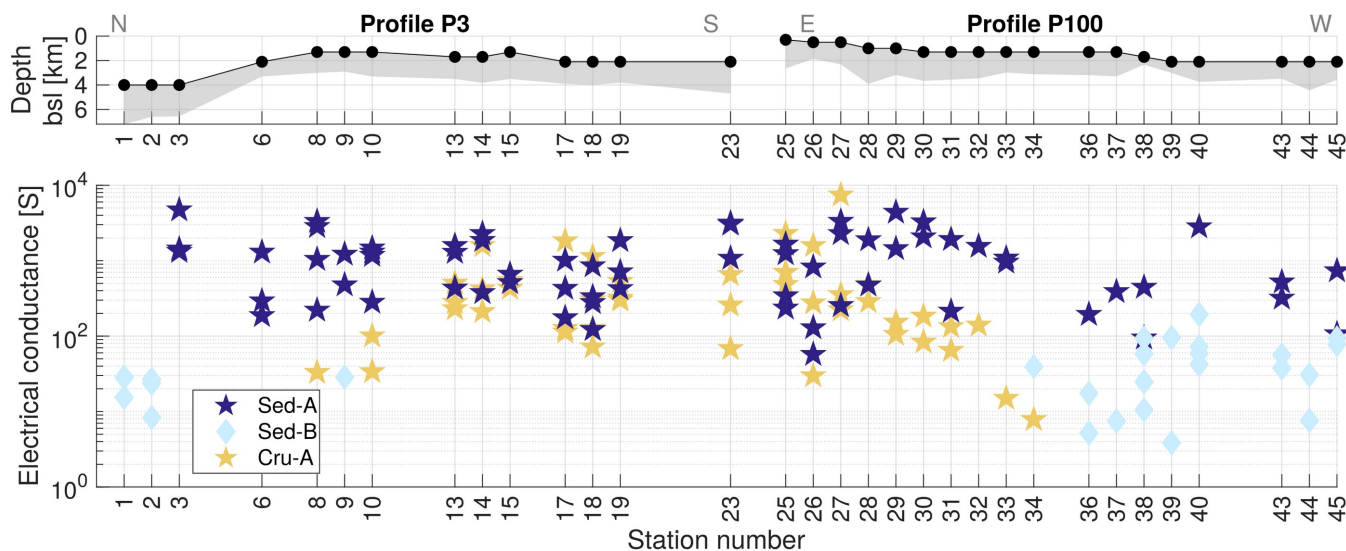
Figure 6: Depiction of the electrical conductance of three shallow clusters. Top panel shows depth of marine MT stations along profiles P3 (stations 1 to 23) and P100 (stations 25 to 45). Grey area shows thickness of seismically derived sediment thickness (Planert et al., 2017 for profile P3, and Fromm et al., 2017a for profile P100). Bottom panel shows the electrical conductance (conductivity-thickness product) of columns below the corresponding MT station for sediment domain clusters sed-A and sed-B, as well as the crustal cluster cru-A.

4.2 Crustal domain

The crustal domain is defined as the region between the defined sediment base (previous section) and the defined Moho. The Gaussian mixture algorithm places four clusters in this domain (cp. Fig. 2), which describe the following four parameter ranges or relationships.

Cluster cru-A (yellow stars in Fig. 3b) summarizes the low electrical resistivity and low density areas of the model. Electrical resistivity is largely below ~50 Ωm and density below circa 2700 kg m^{-3}. The spatial distribution is along the eastern part of profile P100 (stations MT25 – MT32, Fig. 4) and the southern part of profile P3 (stations MT13 – MT23, Fig. 5) and their depth range is less than 9 km below seafloor.

The second cluster cru-B (mint diamonds in Fig. 3b) has the largest variations in terms of parameter ranges and spatial distribution. Electrical resistivity ranges between less than 1 and more than 1000 Ωm, and density values vary from 2500 to 2900 kg m^{-3}. The cluster's cells are distributed in all model areas and summarize mostly shallow ranges above 10 km (e.g. kilometre 180 – 210 on profile P100), but also includes some deep model features (e.g. kilometre 140 – 160 on profile P3).

Cluster cru-C (olive circles in Fig. 3b) combines model cells with well-defined densities around 2750 and 2850 kg m^{-3} and

320 electrical resistivities ranging from ~500 to 20 000 Ωm. The cells are almost exclusively located in the onshore model part and are equally distributed at all depths (0 – 40 km).

The last crustal cluster cru-D (dark green triangles and green squares in Fig. 3b) consists of high resistivity (>100 Ωm), and the highest density (> 2805 kg m^{-3}) values. The cluster's cells are distributed over the entire model area. Interestingly, if the

325 cluster is manually subdivided into a lower and upper resistivity part at 400 Ωm, we obtain a distinct spatial discrimination. Occurrences of "cluster cru-D1", with the high resistivity part, are now constrained to the deeper crust below Walvis Ridge, only. Upper crustal cells over the entire model, and the lower crust south of the ridge are attributed to "cluster cru-D2" (marked as light green squares in Fig. 3b), and exhibit a very similar depth- and spatial distribution as cluster cru-B, with a dominance of cell depths at ~5 – 10 km below seafloor.

330 **4.3 Mantle domain**

The mantle domain comprises all model cells below the defined Moho, all the way to the model's base at 300 km. Due to decreasing sensitivity, we show the model's sections with marked clusters (Figs. 4 and 5) only to a depth of 100 km, but the parameter cross plot (Fig. 3) includes all depths. Gaussian mixture modelling places four distinct parameter clusters, characterized by the following aspects:

335

Cluster man-A (orange stars in Fig. 3c) summarized mostly cluster outliers, with electrical resistivities ranging from exceptionally low values (1 – 10 Ωm) to ~2000 Ωm and density ranging from 3100 to 3300 kg m^{-3}. The associated model cells are mostly located below station MT2, MT3, MT10, and MT23 (Fig. 5). The model areas of these three stations coincides with striking, small-scale low resistivity anomalies across the northern- and southern edge of Walvis Ridge, and

340 the outermost MT station. Model resolution tests for the narrow conductor at ~90 km (coinciding with the Florianopolis fracture zone north of Walvis Ridge) (Franz et al., 2021), have indicated that a shallow anomaly associated with the fracture zone could be severely smeared due to an effect of sudden change in topography or sediment thickness (Garcia et al., 2015; Worzewski et al., 2012), resulting in the artefacts at mantle depths.

345 Cluster man-B (light pink diamonds in Fig. 3c) comprises a cluster of low mantle resistivities (between ~100 and ~400 Ωm) and increased densities of ~3220 to ~3290 kg m^{-3}. The cluster's cells are exclusively located at the MT stations south of Walvis Ridge (MT10-23, Fig. 5) and cover all depth ranges of the mantle (25-300 km).

The third mantle domain cluster, man-C (purple circles in Fig. 3c) comprises resistivity values between ~1000 and ~10 000

350 Ωm and densities around 3220 kg m^{-3}, meaning it is very close to the reference value of 3222 kg m^{-3}. The associated model

14

cells are distributed at the bottom of the model (> 200 km) along Walvis Ridge (MT25-45), as well as in the entire depth range below the onshore stations (MT100-302).

The last parameter cluster of the mantle domain, cluster man-D (dark red triangles in Fig. 3c) encloses high resistivity (>500

355 Ωm), and high density (mostly >3220 kg m^{-3}) cells, which are located all along Walvis Ridge (stations MT25-44 and MT6-9) in shallow and medium mantle depths.

5 Discussion: Link between the identified physical parameter clusters, passive margin evolutionary phases, and associated crustal types

By spatially correlating the defined clusters of all three domains, and comparison to related geophysical models, we have

360 identified a systematic differentiation of the crustal structure from south to north. Thus, we defined three provinces in our survey linked to Walvis Ridge, by distinguishing areas south of, along, and north of the prominent bathymetric high. This zoning also reflects the successive south to north unzipping of the South Atlantic opening, and is related to the evolutionary phases described in Sect. 2.

5.1 Transitional crust south of Walvis Ridge

365 The crust south of Walvis Ridge has previously been characterized by an abrupt change from a continental rift zone to a mainly igneous transitional crust (Bauer et al., 2000; Blaich et al., 2011; Mutter et al., 1988). Extensive sequences of thickened high velocity lower crust, intrusive bodies like dykes and sills, and surface flows in the form of seaward dipping reflectors are representative of this transitional crust (Franke, 2013; Geoffroy, 2005; White & McKenzie, 1989). We attribute the structure inferred from clustering in the southern part of profile P3 (stations MT13 – MT23, Fig. 5) to this series of

370 magmatic activity. It is defined from top to bottom by a) low resistivity, high conductance, low density sediments of cluster sed-A; b) very low resistivity, high conductance, low density upper crust of cluster cru-A, and median resistivity and density mid- to lower crust of clusters cru-B and cru-D. The cells associated with cru-D south of Walvis Ridge can be mostly attributed to the manually defined cluster "cru-D2", which comprises the cells with electrical resistivity <400 Ωm (see Sect. 4.2). The mantle part of the southern transitional crust is exclusively defined by c) lower resistivity and median density

375 values of cluster man-C.

The low resistivity and density values of cluster sed-A below the southern stations MT13 to MT23 likely represent thick sediments. The electrical conductance values of cluster sed-A (~100-5000 S, Fig. 6) are typical for coastal sediments, where the high values are often indicative of increased sediment thickness, but further mechanisms, such as heat flow, or sediment

380 type are relevant as well. (Grayver, 2021). The increased sediment thickness along the post-rift basins of the Namibian margin can be explained with the transport of clastic sediments during the late Cretaceous and early Tertiary (Guillocheau et

al., 2012; Rouby et al., 2009; Stewart et al., 2000). These sediments may have been transported along the shelf by bottom and surface currents and likely originate from cyclic erosion-deposition phases linked to the Orange, Kuiseb, and Swakop rivers (Dingle, 1992; Dingle et al., 1987; Goslin et al., 1974). Furthermore, Gholamrezaie et al. (2018) and Maystrenko et al.

385   (2013) observed increased geothermal gradients in the sediment basins along the margin, which are explained with the effect of "thermal blanketing" through the thick insulating cover. Therefore, increased heat flow in these basins can also be regarded as a potential reason for the high electrical conductance values of cluster sed-A.

Below the assumed sediment base (Planert et al., 2017), the upper crust south of Walvis Ridge is characterized by cluster

390   cru-A. Coast perpendicular seismic profiles published and discussed in Gladczenko et al. (1998) and Eldholm et al. (2000) cross our coast parallel profile P3. Slices along these transects through our 3D resistivity model are overlaid by seismic line drawings of Gladczenko et al. (1998), and show a correspondence of the upper crustal low resistivity anomalies with occurrences of seaward dipping reflectors (Fig. 7). Analysis of boreholes on the Norwegian shelf (ODP104-642 and ODP152-917), describe the SDR series as cyclic sequences of alternating layers of massive basalt flows, weathered or

395   vesicular basalt flows, and volcaniclastic, as well as terrigenous sediments and claystones (Eldholm et al., 1987; Larsen et al., 1994; Planke, 1994; Planke et al., 2000). The downhole geophysical data disclose electrical resistivity values in the range of 5 to 80 Ωm, and densities between 2200 and 2800 kg m^{-3}, with the variation being mostly influenced by the proportions of sediments, weathered-, and massive basalts. These proportions are essentially linked to possible continental sediment input, quantity, and duration of basalt extrusions, as well as the extent of gaps in the extrusion where surface basalts are subject to

400   weathering.

On the East Faroe High and in the Faroe-Shetland Basin, marine electromagnetic studies have imaged conductive sediments with resistivities in the range of ~5 to 30 Ωm below a massive basalt layer (Heincke et al., 2017; Hoversten et al., 2015; Jegen et al., 2009; Panzner et al., 2016). The logging data from the Brugdan and Rosebank wells located along the profiles of

405   these surveys reveal respective resistivity and density values of >100 Ωm and 2600 – 2900 kg m^{-3} for the massive basalts, and 2 – 10 Ωm and 2200 – 2500 kg m^{-3} for the underlying sediment sequence. In further electromagnetic studies at the Norwegian and Australian passive margins, upper crustal conductors have been interpreted as mineral deposits along igneous intrusions or sills (Corseri et al., 2017; Myer et al., 2013), or graphite precipitation along a detachment zone (Heinson et al., 2005). These studies also discuss the difficulty to resolve both conductivity and thickness of the thin, highly conductive

410   mineral layers, and therefore specify electrical conductance values, ranging between $1.5·10^4$ and $3·10^4$ S. This clearly exceeds the values of our resistivity model (mostly ~50 – 2000 S, Fig. 6), pointing at a different conducting mechanism and thus different lithology.

Consequently, we interpret cluster cru-A to represent an anomaly associated with the seaward dipping reflector series,

415   resulting from an interlayering of clastic sediments and volcanic flows following the interpretation of Bauer et al. (2000);

16

Gladczenko et al. (1998); and Koopmann et al. (2016). The conductance values are largely similar to the range observed in the overlying sediments (Fig. 6), which may be indicative for large amounts of sediments or weathered basalts, and few or thin layers of massive basalts, pointing at a periodic extrusive magmatism. The lack of a distinct difference in density between the overlying pure sediment cluster sed-A and the mixed sediment-magmatics cluster cru-A, could be linked to the

420   lack of vertical resolution of the gravity method and a dominant influence of the MT method in the inversion's cross-gradient coupling (Franz et al., 2021) and the increased sensitivity of the MT method for (thin) conductors (Bedrosian, 2007).
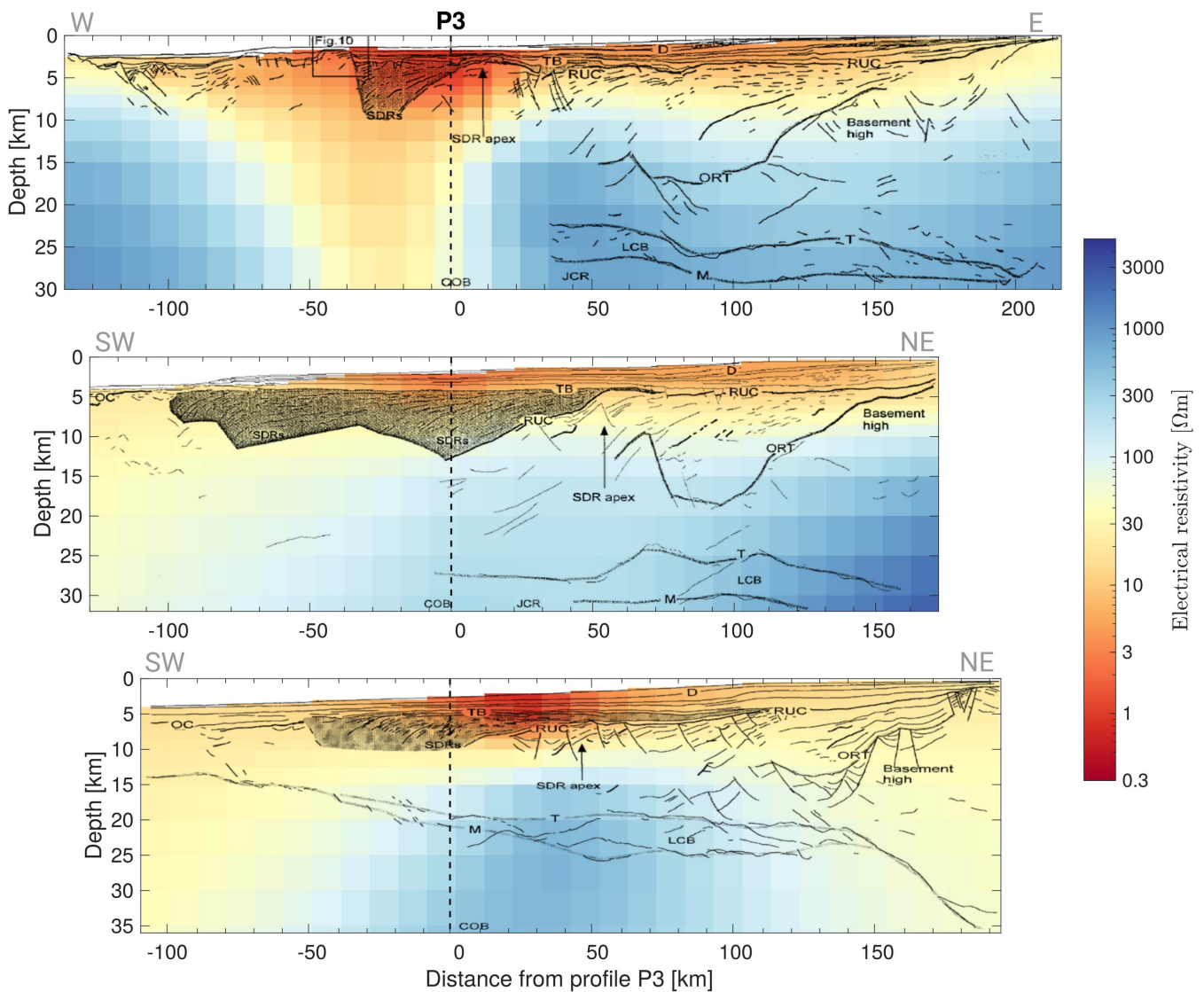
Figure 7: Vertical slices through the 3D resistivity model along seismic transects presented in Gladczenko et al. (1998) overlaid with their lines drawings of MCS data. From top to bottom are their transects 2, 3, and 4 (their Figs. 4 to 6). Location of transects

425   is shown in Fig. 1. Vertical dashed line is the intersection with our profile P3.

17

The middle crust south of Walvis Ridge is assigned to clusters cru-B and cru-D (Fig. 5), where most of the cells associated with cru-D fall into the part of the cluster with electrical resistivity <400 Ωm (referred to as "cluster cru-D2" in Sect. 4.2). The cells associated with cluster cru-B are either situated in the shallow crust or at the transition to conductive features. Therefore, it likely does not characterize a certain lithological unit, but summarized transitional cells due to model smoothing. The evolution from rifted continental- to oceanic crust at the passive margin is characterized by a growing imprint of magmatism into the fractured crust and eventually a purely igneous composition (Blaich et al., 2011; White & McKenzie, 1989). All along the Namibian margin, high mid-crustal velocities (Bauer et al., 2000; Gladczenko et al., 1998; Planert et al., 2017) indicate a mainly igneous composition and the typical rift related structures, for example rotated fault blocks in continental crust, are either lacking (Bauer et al., 2000), or observed closer to the coast (Gladczenko et al., 1998). This indicates a short rifting period with an abrupt continental rupture. At the base of the crust, cumulate bodies and layered intrusions form magmatic underplating, which has been observed along the entire Namibian margin (Bauer et al., 2003; Blaich et al., 2011; Fromm et al., 2017a; Gladczenko et al., 1998; Hirsch et al., 2009; Planert et al., 2017). Cluster "cru-D2" represents increased values for both electrical resistivity and density (~100 – 400 Ωm, and 2700 – 2850 kg m^{-3}) and cells associated with these clusters are distributed in all model parts. We attribute it to the underplated and intruded igneous crust, representing the intrusive counterpart to the extrusive interlayered flows of cru-A.

In the mantle domain, the cluster man-B is remarkably confined, both in the physical parameter space as well as in the spatial extent (Figs. 3 and 5). It clearly clusters all mantle cells of the southern transitional domain. The comparably low resistivity values there could be attributed to a difference in melt source, like a heterogeneous, hydrous source south of Walvis Ridge, compared to a depleted mantle due to volatile extraction by the hot spot source along the ridge (Gardés et al., 2014; Jones et al., 2012; Hirth & Kohlstedt, 1996; Baba et al., 2017). This supports the idea of a mostly rift driven breakup in the southern area, in contrast to a heavily plume influenced breakup at Walvis Ridge latitudes.

5.2 Transitional crust along Walvis Ridge

The transitional crust beneath the landfall of Wavis Ridge has likely been directly impacted by the Tristan mantle plume (Jackson et al., 2000; O'Connor & Duncan, 1990). Therefore, the crust exhibits different characteristics than the southern part, while some mechanisms explained in Sect. 5.1 are similar.

A detailed investigation of the Namibian continental crust's complex composition is not in the scope of this survey, which focuses on the marine environment. Nevertheless, the clusters cru-C and man-C are clearly dominant below the eight onshore MT stations and thus form clusters characteristic for our model's continental regime. Both clusters stand out with particularly high electrical resistivity values and densities which are very close to the reference (2810 kg m^{-3} for the crustal-, and 3222 kg m^{-3} for the mantle domain). Several seismic studies have found high velocities in the lower crust and thickened

18

crust (Heit et al., 2015; Ryberg et al., 2022; Ryberg et al., 2015; Yuan et al., 2017), and interpret it to be an effect of

460 magmatic underplating from the thermal anomaly associated with the Tristan mantle plume arrival. In resistivity studies, cratonic crust is usually expected to have very high electrical resistivities of several thousand Ωm and more (Jones et al., 2009; Moorkamp et al., 2022; Van Zijl, 1977), while mobile belts can show significantly reduced electrical resistivities of ~10 – 50 Ωm (de Beer et al., 1982; Moorkamp et al., 2022; Van Zijl, 1977). The Magnetotelluric studies in the Namibian region have imaged the same behaviour, with very high resistivities in the eastern areas of the Congo craton, and very low

465 resistivity zones in the Kaoko and Damara belts (Kapinos et al., 2016; Khoza et al., 2013; Ritter et al., 2003; Weckmann et al., 2003). Our electrical resistivity model shows uniformly high resistivity values in the majority of the continental crust, with one near-coast conductive zone between 5-10 km depth (Fig. 4, 410 – 470 km), which could be attributed to one or several of the major shear zone of the Kaoko belt (Goscombe et al., 2003).

470 Figure 4 shows, that the eastern marine part of profile P100 (~250 – 370 km) is constructed similar to the southern transitional crust: conductive sediments of cluster sed-A, conductive upper crust interpreted as interlayered sediments and volcanic flows of cluster cru-A, and a cluster cru-D comprising the middle- and lower crust. Directly adjacent to Walvis Ridge, seaward dipping reflectors have been shown to dip to the north instead of the generally westward dipping series along the margin (Elliott et al., 2009; Koopmann et al., 2016). These are attributed to accommodation space created by short-lived

475 subsidence at the interaction of the plume and rifting crust, and may explain the development of cru-A type interlayered sediment – magmatic flow packages along Walvis Ridge, which is in accordance with seismic observations by Fromm et al. (2017a). Strikingly, towards the centre of the magmatic activity below Walvis Ridge (MT stations 8 to 10, and 28 to 34) the conductance values of the crustal cluster cru-A decrease (Fig. 6), while the overlying sediments remain at high conductance. We interpret this to depict an increase in volume of magmatic extrusions, or longer active periods with short breaks. Both

480 result in an increase of massive basalt layers and smaller amounts of conductive sediments or weathered basalts in the seaward dipping reflector series. Another main difference of the transitional crust along Walvis Ridge to that south of the ridge is the absence of the manually defined cluster "cru-D2". While it describes most middle- to lower crustal cells in the southern domain, the middle- to lower crust along profile P100 is entirely composed of cells attributed to the high resistivity (> 400 Ωm) part of cru-D. Once more, we attribute this to a combination of the longer lasting magmatic overprint due to the

485 halted breakup, and to the impingement of the Tristan plume. Both lead to increased magmatic volumes, including crustal intrusions, magmatic underplating, crustal thickening, as well as uplift. The crustal thickness directly below Walvis Ridge reaches ~33 km compared to ~20 – 25 km in the southern part and the thickness of the magmatic underplating is at ~12 km below Walvis Ridge, and ~4-6 km south of it (Fromm et al., 2017a; Goslin & Sibuet, 1975; Planert et al., 2017).

490 Corresponding to the increased crustal resistivity below Walvis Ridge, the mantle underlying Walvis Ridge is also different to the southern transitional mantle (man-B) with significantly higher resistivity and also density values (Fig. 3c, cluster man-D). Sensitivity tests have shown, that high electrical resistivity values need to reach deep into the mantle, yet absolute values

19

are beyond the resolution capabilities of our study (cp. Franz et al., 2021). We attribute these high mantle values to the remnant signature of the upwelling plume, where volatile elements are extracted from melts and rise to the surface to form

495   flood basalts, volcanic flows, and the new oceanic crust (Mutter et al., 1988). The depleted material left in the shallow mantle is highly resistive due to the lack of fluid phases and elements like iron and hydrogen (Baba, 2005; Evans et al., 2005; Matsuno et al., 2010; Selway, 2014).

In contrast to this near-coast part of the profile portraying the heavily magmatically overprinted crust, the western half

500   further offshore (Fig. 4, 0 to ~200 km) exhibits a decreasing influence of breakup related magmatism. The crust is still significantly thicker than normal oceanic crust (up to 20 km, Fromm et al., 2017a; Fromm et al., 2017b) demonstrating the impact of the Tristan plume tail, but it lacks the previously discussed typical upper crustal cluster cru-A representing interlayered sediments and surface volcanic flows. This indicates the transition to submarine spreading and the development of crust corresponding to pillow basalts, sheeted dykes, and gabbros of oceanic layers 2 and 3 but in a thickened, Icelandic

505   type form (Foulger et al., 2003; Fromm et al., 2017a). Furthermore, the sediment domain reveals a seaward change of the assigned cluster from sed-A to sed-B in the same region, also indicating a transition in sediment regime. The cells of cluster sed-B comprise conductance values which are one order of magnitude and more lower than those of cluster sed-A (Fig. 6). Although lower conductance is often attributed to sediment thickness (Grayver, 2021), Fig. 6 (top) shows that along both profiles, the seismically imaged sediment thickness deviates repeatedly around a mean of circa 2 km. Although slight trends

510   of increasing sediment thickness south- and eastwards are observed, clusters sed-A and sed-B can not be clearly correlated to sediment thickness. We have previously mentioned, that vertical model cell size at seafloor depth may be too large (mostly 1 km) to accurately parameterize sediment thickness. To evaluate, whether the clear spatial differentiation of the two sediment clusters is biased by the inappropriately large vertical model cell size or conductivity-thickness ambiguities, we resort to a "reverse" conductance calculation. Namely, we use the exact seismically determined sediment thickness at the location of

515   the MT station to estimate electrical resistivity from the model's conductance values. This reverse calculation results in resistivity values of ~0.5 to 10 Ωm for cluster sed-A, and ~10 to 100 Ωm for cluster sed-B, which confirms the cluster analysis results (Fig. 3). We therefore conclude, that the accuracy of the interpolated sediment thickness based on the model's cell thicknesses is sufficient to differentiate between clusters sed-A and sed-B. After eliminating this source of error, we interpret the two clusters' differentiation to result mainly from the sediment layer's electrical resistivity, which indicates

520   a change in sediment type or sea bottom heat flow (Grayver, 2021). The previously described effect of "thermal blanketing" in the southern Namibe basin (Gholamrezaie et al., 2018; Maystrenko et al., 2013), is likely a factor responsible for the differentiation of the two sediment clusters. This would mean, that the increased resistivity values of cluster sed-B are linked to a decrease in temperature away from the major depositional centre of Walvis Basin. Additionally, a change in sediment type, which could be a decrease in terrigenous input as discussed in Sect. 5.1 as well as a decrease in sediment porosity, can

525   influence the sediment resistivity. Nevertheless, the untypically high absolute sediment resistivity values of cluster sed-B may still be biased by the influence of crustal components.

5.3 Oceanic crust north of Walvis Ridge

Only three MT stations are situated north of the Florianopolis fracture zone (FFZ), with the closest one (MT03) likely experiencing a strong impact of the drastic topography (cp. Franz et al., 2021). Nevertheless, we aim to discuss the crustal
530   composition by using the other available geophysical models, like the information about Moho depth, as reference, in order to infer the full formation history of the Namibian margin.

The main results here are: a) the dominant sediment domain cluster sed-B matching the observation of far offshore sediments along profile P100; and b) the dominant crustal- and mantle clusters cru-D and man-D correlating to the high resistivity-
535   high density clusters observed below Walvis Ridge, but appearing at much shallower depths. Both of these observations indicate a gradual transition to normal oceanic crust, supporting the hypothesis that a ridge jump at the FFZ transferred breakup related crust to the South American side, making the Angolan coast a rather magma-poor margin (Blaich et al., 2011; Franke, 2013). Sediment domain cluster sed-B (Fig. 5, 0 – 70 km), indicates a similarly thin, marine sediment cover as in the far offshore parts on profile P100 (Fig. 4, 0 – 180 km). The thin crust north of Walvis Ridge is mostly assembled in
540   cluster cru-D, while the differentiation in an upper- and lower electrical resistivity cluster, as explained in Sect. 4.2, shows that these cells fall into the lower resistivity cluster "cru-D2". South of Walvis Ridge, we have interpreted this to represent most of the thickened, igneous crust below the extrusive magmatism. However, the observed values are also in accordance with values for normal oceanic crust at the magma-poor margin, i.e. relatively high electrical resistivity (several hundred to >1000 Ωm, cp. Heinson, 1999 and Palshin, 1996) and density (~2800 – 2900 kg m^{-3}, Carlson & Herrick, 1990; Carlson &
545   Raskin, 1984). The difference to the igneous early-stage breakup crust south of Walvis Ridge, is the significantly reduced thickness (5 – 8 km, Goslin & Sibuet, 1975; Planert et al., 2017). This differentiation puts emphasis on the importance of including all available information (here: seismic sections defining crustal thickness), because the MT-gravity joint inversion alone cannot clearly separate the northern- and southern model parts by parameter values only, as they fall into the same cluster "cru-D2". For the mantle domain, the certainty of cluster classification is significantly reduced, illustrated by the
550   decrease in posterior probability of the Gaussian mixture, which is the saturation of symbols in Figs. 3 to 5. The model cells associated with cluster man-D (kilometre 39 to 70 of profile P3) have generally low posterior probability values and are close to an association with cluster man-A, which we have classified as a cluster comprising outliers and artefacts. The Florianopolis fracture zone has a very strong influence on the marine MT data, which significantly distorts our model in this area (cp. Franz et al., 2021). Thus, interpretation of the northern part of our models in the mantle domain should be mostly
555   disregarded.

6 Conclusion

In this study, the clustering and comparison of the rock parameters density and electrical resistivity leads to distinct differentiation of crustal types associated with breakup chronology. Additionally, the resulting parameter correlations may

advance joint inversion of MT and gravity data based on direct parameter coupling, by providing a starting point for cross-
560   property relationships of electrical resistivity and density in the passive margin regime.

Although the evaluation and comparison of different geological and geophysical models in the survey area and comparable regions allows several conclusions about the properties of lithological units, a few factors indubitably limit the parameter classifications. These limitations include the distribution and resolution capabilities of the two data sets and the inversion
565   method, namely, the marine MT station distribution along two 2D profiles; the MT method's insufficient capability to resolve both electrical resistivity and thickness of shallow conductors; the limited sensitivity of unconstrained gravity inversion for the depth of model anomalies, and thus a joint inversion strongly driven by the fitting of the MT data and minimizing the coupling term; and lastly the presumption of a 1D density background model for the calculation of absolute density values (Fig. 3) and the surfaces chosen to differentiate between the three domains.

570

Nevertheless, by focusing the parameter clustering on well constrained model areas, using fuzzy clustering of the Gaussian mixture model method to allow cluster overlaps, and discussing the induced uncertainties of the presumptions, we are able to conclude on the following most striking observed features:

575   1. The differentiation of the sediment domain in a cluster of thick, clastic sediments with increased geothermal gradient, and a second cluster of marine/biogenic sediments. The first (sed-A) occurs mainly at the landfall of Walvis Ridge and south of it and is thus linked to the major depositional centres of the Namibian margin. The second (sed-B) summarizes model areas further away from the shoreline along the ridge and north of it, and represents marine sediments with less terrigenous input.

580

          2. The seismically imaged seaward dipping (SDR) reflectors south of Walvis Ridge show a similar density- and electrical resistivity response as the covering sediment layer. These low density and electrical resistivity values reach up to 9 km into the upper crust, supporting the observation of interlayered sediments and weathered magmatic flows, with either short periods, or lower volume magmatic extrusions. The SDR at the landfall of Walvis Ridge
585   show decreased electrical conductance, which we interpret to depict an increase in magmatic activity towards the centre of magmatic expulsion below Walvis Ridge.

          3. Clustering results in a clear distinction between the response to the magmatic crust south of-, and directly below Walvis Ridge. The crust south of Walvis Ridge is linked to a northward propagating rift, with a mainly igneous
590   composition, layered lower crustal intrusions, and periodic surface volcanic flows (SDR). The crust at the volcanic centre of Walvis Ridge is characterized by accumulation of massive, unweathered magmatics and uplift, and thus

linked to increased and constant magmatic input, as well as a longer accumulation period due to the halted breakup at the Florianopolis fracture zone.

595   4. Additionally, the performed clustering indicates a potentially different upper mantle composition, by assembling the lower-, and upper electrical resistivity clusters man-B, and man-D. Our hypothesis is, that this may result from different melt sources or depth of melting, indicating the differentiation between a rift-related southern complex, and a plume-driven Walvis Ridge regime.

600   From our results, we suppose that Walvis Ridge is an outcome of the combination of halted spreading and the impingement of the Tristan plume. However, the 3D extent of magmatism imaged in our models (which we do not discuss in this article, but in Franz et al., 2021 and Jegen et al., 2016), confirms the observation, that the area of magmatic overprint is too small to justify the arrival of a large plume head (Fromm et al., 2017a; Ryberg et al., 2022). An alternative model explains this smaller scale surface display of the plume by a large, lower mantle upwelling, which tops out at ~1000 km, from where
605   smaller, secondary plumes rise to the surface (Courtillot et al., 2003; French & Romanowicz, 2015; Homrighausen et al., 2019; Zhao, 2007).

With our study, we have defined distinct electrical resistivity – density parameter clusters, linked them with geological units, and compared to multiple independent geological and geophysical models. Our identifications derived from MT and gravity
610   data are corroborated by seismic surveys (e.g. by Fromm et al., 2017; Planert et al., 2017; and Ryberg et al., 2022), pointing to the interesting possibility to derive large scale 3D models through acquisition of 3D MT and joint inversion with satellite gravity data and guiding 2D seismic acquisition.

Author contributions

GF performed formal analysis, and prepared the original draft. MJ provided resources, engaged in conceptualization, data
615   curation, and in manuscript review and editing. MM implemented software, and engaged in manuscript review and editing. CB provided resources, and engaged in conceptualization, visualization, and manuscript review and editing. WR engaged in manuscript review and editing.

Competing interests

The authors declare that they have no conflict of interest.

References

Akaike, H. (1974). A New Look at the Statistical Model Identification. IEEE Transactions on Automatic Control, 19(6), 716–723. https://doi.org/10.1109/TAC.1974.1100705

Anderson, D. L. (2001). Top-Down Tectonics? Science, 293(5537), 2016–2018. https://doi.org/10.1126/science.1065448

Aslanian, D., Moulin, M., Olivet, J. L., Unternehr, P., Matias, L., Bache, F., et al. (2009). Brazilian and African passive margins of the Central Segment of the South Atlantic Ocean: Kinematic constraints. Tectonophysics, 468(1–4), 98–112. https://doi.org/10.1016/j.tecto.2008.12.016

Astic, T., Heagy, L. J., & Oldenburg, D. W. (2020). Petrophysically and geologically guided multi-physics inversion using a dynamic Gaussian mixture model. Geophysical Journal International, 224(1), 40–68. https://doi.org/10.1093/gji/ggaa378

Astic, T., & Oldenburg, D. W. (2019). A framework for petrophysically and geologically guided geophysical inversion using a dynamic Gaussian mixture model prior. Geophysical Journal International, 219(3), 1989–2012. https://doi.org/10.1093/gji/ggz389

Baba, K. (2005). Electrical structure in marine tectonic settings. Surveys in Geophysics, 26(6), 701–731. https://doi.org/10.1007/s10712-005-1831-2

Baba, K., Chen, J., Sommer, M., Utada, H., Geissler, W. H., Jokat, W., & Jegen, M. (2017). Marine magnetotellurics imaged no distinct plume beneath the Tristan da Cunha hotspot in the southern Atlantic Ocean. Tectonophysics, 716, 52–63. https://doi.org/10.1016/j.tecto.2016.09.033

Bauer, K, & Schulze, A. (1996). Seismic investigations of the passive continental margin of Namibia from wide-angle on-shore off-shore data. EOS Trans AGU, 77, F669.

Bauer, K, Neben, S., Schreckenberger, B., Emmermann, R., Hinz, K., Fechner, N., et al. (2000). Deep structure of the Namibia continental margin as derived from integrated geophysical studies. Journal of Geophysical Research: Solid Earth, 105(B11), 25829–25853. https://doi.org/10.1029/2000jb900227

Bauer, K., Trumbull, R. B., & Vietor, T. (2003). Geophysical images and a crustal model of intrusive structures beneath the Messum ring complex, Namibia. Earth and Planetary Science Letters, 216(1), 65–80. https://doi.org/10.1016/S0012-821X(03)00486-2

Becker, K., Franke, D., Trumbull, R., Schnabel, M., Heyde, I., Schreckenberger, B., Koopmann, H., Bauer, K., Jokat, W., &
655   Krawczyk, C. M. (2014). Asymmetry of high-velocity lower crust on the South Atlantic rifted margins and implications for the interplay of magmatism and tectonics in continental breakup. Solid Earth, 5(2), 1011–1026. https://doi.org/10.5194/se-5-1011-2014

Bedrosian, P. A. (2007). MT+, integrating magnetotellurics to determine earth structure, physical state, and processes. Surveys in Geophysics, 28(2–3), 121–167. https://doi.org/10.1007/s10712-007-9019-6

660   de Beer, J. H., Huyssen, R. M. J., Joubert, S. J., & van Zijl, J. S. V. (1982). Magnetometer array studies and deep Schlumberger soundings in the Damara orogenic belt, South West Africa. Geophysical Journal International, 70(1), 11–29. https://doi.org/10.1111/j.1365-246X.1982.tb06388.x

Begg, G. C., Griffin, W. L., Natapov, L. M., O'Reilly, S. Y., Grand, S. P., O'Neill, C. J., et al. (2009). The lithospheric architecture of Africa: Seismic tomography, mantle petrology, and tectonic evolution. Geosphere, 5(1), 23–50.
665   https://doi.org/10.1130/GES00179.1

Blaich, O. A., Faleide, J. I., & Tsikalas, F. (2011). Crustal breakup and continent-ocean transition at South Atlantic conjugate margins. Journal of Geophysical Research: Solid Earth, 116(1), 1–38. https://doi.org/10.1029/2010JB007686

Burke, K., & Dewey, J. F. (1973). Plume-Generated Triple Junctions: Key Indicators in Applying Plate Tectonics to Old Rocks. The Journal of Geology, 81(4), 406–433. https://doi.org/10.1086/627882

670   Carlson, R. L., & Herrick, C. N. (1990). Densities and porosities in the oceanic crust and their variations with depth and age. Journal of Geophysical Research, 95(B6), 9153–9170. https://doi.org/10.1029/JB095iB06p09153

Carlson, R. L., & Raskin, G. S. (1984). Density of the ocean crust. Nature, 311(5986), 555–558. https://doi.org/10.1038/311555a0

Clemson, J., Cartwright, J., & Booth, J. (1997). Structural segmentation and the influence of basement structure on the
675   Namibian passive margin. Journal of the Geological Society, 154(3), 477–482. https://doi.org/10.1144/gsjgs.154.3.0477

Collier, J. S., McDermott, C., Warner, G., Gyori, N., Schnabel, M., McDermott, K., & Horn, B. W. (2017). New constraints on the age and style of continental breakup in the South Atlantic from magnetic anomaly data. Earth and Planetary Science Letters, 477, 27–40. https://doi.org/10.1016/j.epsl.2017.08.007

Corseri, R., Senger, K., Selway, K., Abdelmalak, M. M., Planke, S., & Jerram, D. A. (2017). Magnetotelluric evidence for
680   massive sulphide mineralization in intruded sediments of the outer Vøring Basin, mid-Norway. Tectonophysics, 706–707, 196–205. https://doi.org/10.1016/j.tecto.2017.04.011

Courtillot, V., Davaille, A., Besse, J., & Stock, J. (2003). Three distinct types of hotspots in the Earth's mantle. Earth and Planetary Science Letters, 205(3–4), 295–308. https://doi.org/10.1016/S0012-821X(02)01048-8

Dingle, R. V. (1992). Structural and sedimentary development of the continental margin off southwestern Africa.
685   Communications of the Geological Survey of Namibia, 8(1982), 37–46.

Dingle, R. V., Birch, G. F., Bremner, J. M., De Decker, R., Du Plessis, A., Engelbrecht, J., et al. (1987). Deep sea
sedimentary environments around southern Africa (South-East Atlantic and South- West Indian Oceans). Annals of the
South African Museum, 98(1), 1–27.

Duncan, A. R., Newton, S. R., van den Berg, C., & Reid, D. L. (1989). Geochemistry and petrology of dolerite sills in the
690   Huab River Valley, Damaraland, north-western Namibia. Communications of the Geological Survey of Namibia, 5, 5–17.

Eldholm, O., Thiede, J., Taylor, E., & Al., E. (1987). Proceedings of the Ocean Drilling Program, 104 Initial Reports. (O.
Eldholm, J. Thiede, & E. Taylor, Eds.) (Vol. 104). Ocean Drilling Program. https://doi.org/10.2973/odp.proc.ir.104.1987

Eldholm, O., Gladczenko, T. P., Skogseid, J., & Planke, S. (2000). Atlantic volcanic margins: A comparative study.
Geological Society Special Publication, 167, 411–428. https://doi.org/10.1144/GSL.SP.2000.167.01.16

695   Elliott, G. M., Berndt, C., & Parson, L. M. (2009). The SW African volcanic rifted margin and the initiation of the Walvis
Ridge, South Atlantic. Marine Geophysical Researches, 30(3), 207–214. https://doi.org/10.1007/s11001-009-9077-x

Evans, R. L., Hirth, G., Baba, K., Forsyth, D., Chave, A., & Mackie, R. (2005). Geophysical evidence from the MELT area
for compositional controls on oceanic plates. Nature, 437(7056), 249–252. https://doi.org/10.1038/nature04014

Ferguson, I. J., Lilley, F. E. M., & Filloux, J. H. (1990). Geomagnetic induction in the Tasman Sea and electrical
700   conductivity structure beneath the Tasman Seafloor. Geophysical Journal International, 102(2), 299–312.
https://doi.org/10.1111/j.1365-246X.1990.tb04468.x

Foulger, G. R., Du, Z., & Julian, B. R. (2003). Icelandic-type crust. Geophysical Journal International, 155(2), 567–590.
https://doi.org/10.1046/j.1365-246X.2003.02056.x

Foulger, Gillian R. (2010). Plates vs. Plumes: A Geological Controversy. Plates vs. Plumes: A Geological Controversy. John
705   Wiley & Sons. https://doi.org/10.1002/9781444324860

Franke, D. (2013). Rifting, lithosphere breakup and volcanism: Comparison of magma-poor and volcanic rifted margins.
Marine and Petroleum Geology, 43, 63–87. https://doi.org/10.1016/j.marpetgeo.2012.11.003

Franke, D., Neben, S., Ladage, S., Schreckenberger, B., & Hinz, K. (2007). Margin segmentation and volcano-tectonic
architecture along the volcanic margin off Argentina/Uruguay, South Atlantic. Marine Geology, 244(1–4), 46–67.
710   https://doi.org/10.1016/j.margeo.2007.06.009

Franz, G., Moorkamp, M., Jegen, M., Berndt, C., & Rabbel, W. (2021). Comparison of Different Coupling Methods for Joint
Inversion of Geophysical Data: A Case Study for the Namibian Continental Margin. Journal of Geophysical Research:
Solid Earth, 126(12), 1–28. https://doi.org/10.1029/2021jb022092

French, S. W., & Romanowicz, B. (2015). Broad plumes rooted at the base of the Earth's mantle beneath major hotspots.
715   Nature, 525(7567), 95–99. https://doi.org/10.1038/nature14876

Frimmel, H. E. (2009). Configuration of Pan-African Orogenic Belts in Southwestern Africa. In C. Gaucher, A. N. Sial, G.
P. Halverson, & H. E. Frimmel (Eds.), Developments in Precambrian Geology: Neoproterozoic-Cambrian Tectonics,

26

Global Change and Evolution: A Focus on South Western Gondwana (pp. 145–151). Elsevier. https://doi.org/10.1016/S0166-2635(09)01610-7

720 Fromm, T, Jokat, W., Ryberg, T., Behrmann, J. H., Haberland, C., & Weber, M. (2017a). The onset of Walvis Ridge: Plume influence at the continental margin. Tectonophysics, 716, 90–107. https://doi.org/10.1016/j.tecto.2017.03.011

Fromm, T., Jokat, W., & Behrmann, J. H. (2017b). Interaction between a hotspot and a fracture zone: The crustal structure of Walvis Ridge at 6° E. Tectonophysics, 716, 108–120. https://doi.org/10.1016/j.tecto.2017.03.001

Fromm, T., Planert, L., Jokat, W., Ryberg, T., Behrmann, J. H., Weber, M. H., & Haberland, C. (2015). South Atlantic
725 opening: A plume-induced breakup? Geology, 43(10), 931–934. http://dx.doi.org/10.1130/g36936.1

Garcia, X., Seillé, H., Elsenbeck, J., Evans, R. L., Jegen, M., Hölz, S., et al. (2015). Structure of the mantle beneath the Alboran Basin from magnetotelluric soundings. Geochemistry, Geophysics, Geosystems. https://doi.org/10.1002/2015GC006100

Gardés, E., Gaillard, F., & Tarits, P. (2014). Toward a unified hydrous olivine electrical conductivity law. Geochemistry,
730 Geophysics, Geosystems, 15(12), 4984–5000. https://doi.org/10.1002/2014GC005496

Gassmöller, R., Dannberg, J., Bredow, E., Steinberger, B., & Torsvik, T. H. (2016). Major influence of plume-ridge interaction, lithosphere thickness variations, and global mantle flow on hotspot volcanism – The example of Tristan. Geochemistry, Geophysics, Geosystems, 17(4), 1454–1479. https://doi.org/10.1002/2015GC006177

Geoffroy, L. (2005). Volcanic passive margins. Comptes Rendus – Geoscience, 337(16), 1395–1408.
735 https://doi.org/10.1016/j.crte.2005.10.006

Georgen, J. E., & Lin, J. (2001). The effects of transform faults on along-axis flow of plume material: Implications for plume-ridge interaction. In Interactions between mantle plumes and mid-ocean ridges: Constraints from geophysics, geochemistry, and geodynamical modeling (Dissertation).

Gernigon, L., Ringenbach, J. C., Planke, S., & Le Gall, B. (2004). Deep structures and breakup along volcanic rifted
740 margins: Insights from integrated studies along the outer Vøring Basin (Norway). Marine and Petroleum Geology, 21(3), 363–372. https://doi.org/10.1016/j.marpetgeo.2004.01.005

Géron, A. (2019). Hands-on machine learning with Scikit-Learn, Keras and TensorFlow: concepts, tools, and techniques to build intelligent systems. (R. Roumeliotis & N. Tache, Eds.) (2. Edition). O'Reilly.

Gholamrezaie, E., Scheck-Wenderoth, M., Sippel, J., & Strecker, M. R. (2018). Variability of the geothermal gradient across
745 two differently aged magma-rich continental rifted margins of the Atlantic Ocean: The Southwest African and the Norwegian margins. Solid Earth, 9(1), 139–158. https://doi.org/10.5194/se-9-139-2018

Gladczenko, T. P., Skogseid, J., & Eldhom, O. (1998). Namibia volcanic margin. Marine Geophysical Research, 20(4), 313–341. https://doi.org/10.1023/A:1004746101320

Glen, J. M. G., Renne, P. R., Milner, S. C., & Coe, R. S. (1997). Magma flow inferred from anisotropy of magnetic
750 susceptibility in the coastal Paraná-Etendeka igneous province: Evidence for rifting before flood volcanism. Geology, 25(12), 1131–1134. https://doi.org/10.1130/0091-7613(1997)025<1131:MFIFAO>2.3.CO;2

Goscombe, B., Hand, M., & Gray, D. (2003). Structure of the Kaoko Belt, Namibia: Progressive evolution of a classic transpressional orogen. Journal of Structural Geology, 25(7), 1049–1081. https://doi.org/10.1016/S0191-8141(02)00150-5

Goslin, J., & Sibuet, J. C. (1975). Geophysical study of the easternmost Walvis Ridge, South Atlantic: Deep structure.

755   Bulletin of the Geological Society of America, 86(12), 1713–1724. https://doi.org/10.1130/0016-7606(1975)86<1713:GSOTEW>2.0.CO;2

Goslin, J., Mascle, J., Sibuet, J.-C., & Hoskins, H. (1974). Geophysical study of the easternmost Walvis Ridge, South Atlantic: Morphology and shallow structure. Geological Society of America Bulletin, 85(4), 619–632. https://doi.org/10.1130/0016-7606(1974)85<619:GSOTEW>2.0.CO;2

760   Grayver, A. V. (2021). Global 3-D Electrical Conductivity Model of the World Ocean and Marine Sediments. Geochemistry, Geophysics, Geosystems, 22(9). https://doi.org/10.1029/2021GC009950

Guillocheau, F., Rouby, D., Robin, C., Helm, C., Rolland, N., Le Carlier de Veslud, C., & Braun, J. (2012). Quantification and causes of the terrigeneous sediment budget at the scale of a continental margin: A new method applied to the Namibia-South Africa margin. Basin Research, 24(1), 3–30. https://doi.org/10.1111/j.1365-2117.2011.00511.x

765   Haas, P., Ebbing, J., Celli, N. L., & Rey, P. F. (2021). Two-step Gravity Inversion Reveals Variable Architecture of African Cratons. Frontiers in Earth Science, 9(December), 1–14. https://doi.org/10.3389/feart.2021.696674

Harris, C., Marsh, J. S., & Milner, S. C. (1999). Petrology of the alkaline core of the messum igneous complex, Namibia: Evidence for the progressively decreasing effect of crustal contamination. Journal of Petrology, 40(9), 1377–1397. https://doi.org/10.1093/petroj/40.9.1377

770   Heincke, B., Jegen, M., Moorkamp, M., Hobbs, R. W., & Chen, J. (2017). An adaptive coupling strategy for joint inversions that use petrophysical information as constraints. In Journal of Applied Geophysics (Vol. 136, pp. 279–297). Society of Exploration Geophysicists. https://doi.org/10.1016/j.jappgeo.2016.10.028

Heine, C., Zoethout, J., & Müller, R. D. (2013). Kinematics of the South Atlantic rift. Solid Earth, 4(2), 215–253. https://doi.org/10.5194/se-4-215-2013

775   Heinson, G. (1999). Electromagnetic studies of the lithosphere and asthenosphere. Surveys in Geophysics, 20(3–4), 229–255. https://doi.org/https://doi.org/10.1023/A:1006689521329

Heinson, G., White, A., & Lilley, F. E. M. (2005). Rifting of a passive margin and development of a lower-crustal detachment zone: Evidence from marine magnetotellurics. Geophysical Research Letters, 32(12), 1–4. https://doi.org/10.1029/2005GL022934

780   Heit, B., Yuan, X., Weber, M., Geissler, W., Jokat, W., Lushetile, B., & Hoffmann, K. H. (2015). Crustal thickness and Vp/Vs ratio in NW Namibia from receiver functions: Evidence for magmatic underplating due to mantle plume-crust interaction. Geophysical Research Letters, 42(9), 3330–3337. https://doi.org/10.1002/2015GL063704

Hinze, W. J., von Frese, R. R. B., & Saad, A. H. (2013). Density of Earth materials. In Gravity and Magnetic Exploration (pp. 64–87). Cambridge: Cambridge University Press. https://doi.org/10.1017/CBO9780511843129.005

785   Hirth, G., & Kohlstedt, D. L. (1996). Water in the oceanic upper mantle: implications for rheology, melt extraction and the evolution of the lithosphere. Earth and Planetary Science Letters, 144(1–2), 93–108. https://doi.org/10.1016/0012-821X(96)00154-9

Hirsch, K. K., Bauer, K., & Scheck-Wenderoth, M. (2009). Deep structure of the western South African passive margin – Results of a combined approach of seismic, gravity and isostatic investigations. Tectonophysics, 470(1–2), 57–70.
790   https://doi.org/10.1016/j.tecto.2008.04.028

Homrighausen, S., Hoernle, K., Hauff, F., Wartho, J. A., van den Bogaard, P., & Garbe-Schönberg, D. (2019). New age and geochemical data from the Walvis Ridge: The temporal and spatial diversity of South Atlantic intraplate volcanism and its possible origin. Geochimica et Cosmochimica Acta, 245, 16–34. https://doi.org/10.1016/j.gca.2018.09.002

Hoversten, G. M., Myer, D., Key, K., Alumbaugh, D., Hermann, O., & Hobbet, R. (2015). Field test of sub-basalt
795   hydrocarbon exploration with marine controlled source electromagnetic and magnetotelluric data. Geophysical Prospecting, 63(5), 1284–1310. https://doi.org/10.1111/1365-2478.12278

Jackson, M. P. A., Cramez, C., & Fonck, J. M. (2000). Role of subaerial volcanic rocks and mantle plumes in creation of South Atlantic margins: Implications for salt tectonics and source rocks. Marine and Petroleum Geology, 17(4), 477–498. https://doi.org/10.1016/S0264-8172(00)00006-4

800   Jegen, M., Hobbs, R. W., Tarits, P., & Chave, A. D. p. (2009). Joint inversion of marine magnetotelluric and gravity data incorporating seismic constraints. Preliminary results of sub-basalt imaging off the Faroe Shelf. Earth and Planetary Science Letters, 282(1–4), 47–55. https://doi.org/10.1016/j.epsl.2009.02.018

Jegen, M., Avdeeva, A., Berndt, C., Franz, G., Heincke, B., Hölz, S., et al. (2016). 3-D magnetotelluric image of offshore magmatism at the Walvis Ridge and rift basin. Tectonophysics, 683, 98–108. https://doi.org/10.1016/j.tecto.2016.06.016

805   Jones, A. G., Evans, R. L., & Eaton, D. W. (2009). Velocity-conductivity relationships for mantle mineral assemblages in Archean cratonic lithosphere based on a review of laboratory data and Hashin-Shtrikman extremal bounds. Lithos, 109(1–2), 131–143. https://doi.org/10.1016/j.lithos.2008.10.014

Jones, A. G., Fullea, J., Evans, R. L., & Muller, M. R. (2012). Water in cratonic lithosphere: Calibrating laboratory-determined models of electrical conductivity of mantle minerals using geophysical and petrological observations.
810   Geochemistry, Geophysics, Geosystems, 13(6). https://doi.org/10.1029/2012GC004055

Kapinos, G., Weckmann, U., Jegen-Kulcsar, M., Meqbel, N., Neska, A., Katjiuongua, T. T., et al. (2016). Electrical resistivity image of the South Atlantic continental margin derived from onshore and offshore magnetotelluric data. Geophysical Research Letters, 43(1), 154–160. https://doi.org/10.1002/2015GL066811

Keiding, J. K., Frei, O., Renno, A. D., Veksler, I. V., & Trumbull, R. B. (2013). Conditions of magma crystallization in the
815   henties bay-outjo dyke swarm, namibia: Implications for the feeder system of continental flood basalts. Lithos, 179, 16–27. https://doi.org/10.1016/j.lithos.2013.07.018

Key, K., & Constable, S. (2011). Coast effect distortion of marine magnetotelluric data: Insights from a pilot study offshore northeastern Japan. Physics of the Earth and Planetary Interiors, 184(3–4), 194–207. https://doi.org/10.1016/j.pepi.2010.11.008

820 Khoza, T. D., Jones, A. G., Muller, M. R., Evans, R. L., Miensopust, M. P., & Webb, S. J. (2013). Lithospheric structure of an Archean craton and adjacent mobile belt revealed from 2-D and 3-D inversion of magnetotelluric data: Example from southern Congo craton in northern Namibia. Journal of Geophysical Research: Solid Earth, 118(8), 4378–4397. https://doi.org/10.1002/jgrb.50258

Koopmann, H., Schreckenberger, B., Franke, D., Becker, K., & Schnabel, M. (2016). The late rifting phase and continental
825 break-up of the southern South Atlantic: the mode and timing of volcanic rifting and formation of earliest oceanic crust. Geological Society, London, Special Publications, 420(1), 315–340. https://doi.org/10.1144/SP420.2

Koopmann, Hannes, Brune, S., Franke, D., & Breuer, S. (2014). Linking rift propagation barriers to excess magmatism at volcanic rifted margins. Geology, 42(12), 1071–1074. https://doi.org/10.1130/G36085.1

Larsen, H. C., Saunders, A. D., Clift, P. D., & Al., E. (1994). Proceedings of the Ocean Drilling Program, 152 Initial
830 Reports. (H. C. Larsen, A. D. Saunders, & P. D. Clift, Eds.) (Vol. 152). Ocean Drilling Program. https://doi.org/10.2973/odp.proc.ir.152.1994

Laske, G., Masters, G., Ma, Z., & Pasyanos, M. (2013). Update on CRUST1.0 – A 1-degree global model of Earth's crust. In EGU General Assembly 2013 (Vol. 15, p. 2658). Vienna. Retrieved from http://meetingorganizer.copernicus.org/EGU2013/EGU2013-2658.pdf

835 Lelièvre, P. G., Farquharson, C. G., & Hurich, C. A. (2012). Joint inversion of seismic traveltimes and gravity data on unstructured grids with application to mineral exploration. Geophysics, 77(1), K1--K15. https://doi.org/10.1190/1.3513182

Macdonald, D., Gomez-Perez, I., Franzese, J., Spalletti, L., Lawver, L., Gahagan, L., et al. (2003). Mesozoic break-up of SW Gondwana: Implications for regional hydrocarbon potential of the southern South Atlantic. Marine and Petroleum
840 Geology, 20(3–4), 287–308. https://doi.org/10.1016/S0264-8172(03)00045-X

Matsuno, T., Seama, N., Evans, R. L., Chave, A. D., Baba, K., White, A., et al. (2010). Upper mantle electrical resistivity structure beneath the central Mariana subduction system. Geochemistry, Geophysics, Geosystems, 11(9), 1–24. https://doi.org/10.1029/2010GC003101

Maystrenko, Y. P., Scheck-Wenderoth, M., Hartwig, A., Anka, Z., Watts, A. B., Hirsch, K. K., & Fishwick, S. (2013).
845 Structural features of the Southwest African continental margin according to results of lithosphere-scale 3D gravity and thermal modelling. Tectonophysics, 604, 104–121. https://doi.org/10.1016/j.tecto.2013.04.014

McLachlan, G. J., Lee, S. X., & Rathnayake, S. I. (2019). Finite Mixture Models. Annual Review of Statistics and Its Application, 6(1), 355–378. https://doi.org/10.1146/annurev-statistics-031017-100325

Mjelde, R., Raum, T., Murai, Y., & Takanami, T. (2007). Continent-ocean-transitions: Review, and a new tectono-magmatic

850   model of the Vøring Plateau, NE Atlantic. Journal of Geodynamics, 43(3), 374–392.
       https://doi.org/10.1016/j.jog.2006.09.013

Moorkamp, M. (2017). Integrating Electromagnetic Data with Other Geophysical Observations for Enhanced Imaging of the
       Earth: A Tutorial and Review. Surveys in Geophysics, 38(5), 935–962. https://doi.org/10.1007/s10712-017-9413-7

Moorkamp, M. (2022). Deciphering the State of the Lower Crust and Upper Mantle With Multi-Physics Inversion.

855   Geophysical Research Letters, 49(9). https://doi.org/10.1029/2021GL096336

Moorkamp, M., Heincke, B., Jegen, M., Roberts, A. W., & Hobbs, R. W. (2011). A framework for 3-D joint inversion of
       MT, gravity and seismic refraction data. Geophysical Journal International, 184(1), 477–493.
       https://doi.org/10.1111/j.1365-246X.2010.04856.x

Moorkamp, M., Özaydın, S., Selway, K., & Jones, A. G. (2022). Probing the Southern African Lithosphere With

860   Magnetotellurics—Part I: Model Construction. Journal of Geophysical Research: Solid Earth, 127(3).
       https://doi.org/10.1029/2021JB023117

Morgan, W. J. (1971). Convection Plumes in the Lower Mantle. Nature, 230(5288), 42–43.
       https://doi.org/10.1038/230042a0

Moulin, M., Aslanian, D., & Unternehr, P. (2010). A new starting point for the South and Equatorial Atlantic Ocean. Earth-

865   Science Reviews, 98(1–2), 1–37. https://doi.org/10.1016/j.earscirev.2009.08.001

Mutter, J. C., Talwani, M., & Stoffa, P. L. (1982). Origin of seaward-dipping reflectors in oceanic crust off the Norwegian
       margin by "subaerial sea-floor spreading". Geology, 10(7), 353–357. https://doi.org/10.1130/0091-
       7613(1982)10<353:OOSRIO>2.0.CO;2

Mutter, John C., Buck, W. R., & Zehnder, C. M. (1988). Convective partial melting: 1. A model for the formation of thick

870   basaltic sequences during the initiation of spreading. Journal of Geophysical Research, 93(B2), 1031.
       https://doi.org/10.1029/JB093iB02p01031

Myer, D., Constable, S., & Key, K. (2013). Magnetotelluric evidence for layered mafic intrusions beneath the vøring and
       exmouth rifted margins. Physics of the Earth and Planetary Interiors, 220, 1–10.
       https://doi.org/10.1016/j.pepi.2013.04.007

875   Nürnberg, D., & Müller, R. D. (1991). The tectonic evolution of the South Atlantic from Late Jurassic to present.
       Tectonophysics, 191(1–2), 27–53. https://doi.org/10.1016/0040-1951(91)90231-G

O'Connor, J. M., & Duncan, R. A. (1990). Evolution of the Walvis Ridge-Rio Grande Rise Hot Spot System: Implications
       for African and South American Plate motions over plumes. Journal of Geophysical Research: Solid Earth, 95(B11),
       17475–17502. https://doi.org/10.1029/JB095iB11p17475

880   Owen-Smith, T. M., Ashwal, L. D., Sudo, M., & Trumbull, R. B. (2017). Age and petrogenesis of the Doros Complex,
       Namibia, and implications for early plume-derived melts in the Paraná-Etendeka LIP. Journal of Petrology, 58(3), 423–
       442. https://doi.org/10.1093/petrology/egx021

31

Paasche, H., & Tronicke, J. (2007). Cooperative inversion of 2D geophysical data sets: A zonal approach based on fuzzy c-means cluster analysis. Geophysics, 72(3), 35–39. https://doi.org/10.1190/1.2670341

885   Palshin, N. A. (1996). Oceanic electromagnetic studies: A review. Surveys in Geophysics, 17(4), 455–491. https://doi.org/10.1007/BF01901641

Panzner, M., Morten, J. P., Weibull, W. W., & Arntsen, B. (2016). Integrated seismic and electromagnetic model building applied to improve subbasalt depth imaging in the Faroe-Shetland Basin. Geophysics, 81(1), E57–E68. https://doi.org/10.1190/geo2015-0137.1

890   Parker, R. L. (1980). The inverse problem of electromagnetic induction: Existence and construction of solutions based on incomplete data. Journal of Geophysical Research: Solid Earth, 85(B8), 4421–4428. https://doi.org/10.1029/JB085iB08p04421

Passchier, C. W., Trouw, R. A. J., Ribeiro, A., & Paciullo, F. V. P. (2002). Tectonic evolution of the southern Kaoko belt, Namibia. Journal of African Earth Sciences, 35(1), 61–75. https://doi.org/10.1016/S0899-5362(02)00030-1

895   Paton, D. A., Pindell, J., McDermott, K., Bellingham, P., & Horn, B. (2017). Evolution of seaward-dipping reflectors at the onset of oceanic crust formation at volcanic passive margins: Insights from the South Atlantic. Geology, 45(5), 439–442. https://doi.org/10.1130/G38706.1

Peate, D. W. (1997). The Paraná-Etendeka Province. In Large Igneous Provinces: Continental, Oceanic, and Planetary Flood Volcanism (pp. 217–245). https://doi.org/10.1029/GM100p0217

900   Pérez-Gussinyé, M., & Reston, T. J. (2001). Rheological evolution during extension at nonvolcanic rifted margins: Onset of serpentinization and development of detachments leading to continental breakup. Journal of Geophysical Research: Solid Earth, 106(B3), 3961–3975. https://doi.org/10.1029/2000JB900325

Planert, L., Behrmann, J., Jokat, W., Fromm, T., Ryberg, T., Weber, M., & Haberland, C. (2017). The wide-angle seismic image of a complex rifted margin, offshore North Namibia: Implications for the tectonics of continental breakup.

905   Tectonophysics, 716, 130–148. https://doi.org/10.1016/j.tecto.2016.06.024

Planke, S. (1994). Geophysical response of flood basalts from analysis of wire line logs: Ocean Drilling Program Site 642, Vøring volcanic margin. Journal of Geophysical Research: Solid Earth, 99(B5), 9279–9296. https://doi.org/10.1029/94JB00496

Planke, S., Symonds, P. A., Alvestad, E., & Skogseid, J. (2000). Seismic volcanostratigraphy of large-volume basaltic
910   extrusive complexes on rifted margins. Journal of Geophysical Research: Solid Earth, 105(B8), 19335–19351. https://doi.org/10.1029/1999jb900005

Rabinowitz, P. D., & Labrecque, J. (1979). The Mesozoic South Atlantic ocean and evolution of its continental margins. Journal of Geophysical Research, 84(B11), 5973–6002. https://doi.org/10.1029/JB084iB11p05973

Ritter, O., Weckmann, U., Vietor, T., & Haak, V. (2003). A magnetotelluric study of the Damara Belt in Namibia 1.
915   Regional scale conductivity anomalies. Physics of the Earth and Planetary Interiors, 138(2), 71–90. https://doi.org/10.1016/S0031-9201(03)00078-5

Rouby, D., Bonnet, S., Guillocheau, F., Gallagher, K., Robin, C., Biancotto, F., et al. (2009). Sediment supply to the Orange sedimentary system over the last 150 My: An evaluation from sedimentation/denudation balance. Marine and Petroleum Geology, 26(6), 782–794. https://doi.org/10.1016/j.marpetgeo.2008.08.004

920   Ryberg, T, Geissler, W. H., Jokat, W., Yuan, X., Fromm, T., Pandey, S., & Heit, B. (2022). Crustal and uppermost mantle structure of the NW Namibia continental margin and the Walvis Ridge derived from ambient seismic noise. Geophysical Journal International, 230(1), 377–391. https://doi.org/10.1093/gji/ggac084

Ryberg, Trond, Haberland, C., Haberlau, T., Weber, M. H., Bauer, K., Behrmann, J. H., & Jokat, W. (2015). Crustal structure of northwest Namibia: Evidence for plume-rift-continent interaction. Geology, 43(8), 739–742.
925   https://doi.org/10.1130/G36768.1

Salomon, E., Passchier, C., & Koehn, D. (2017). Asymmetric continental deformation during South Atlantic rifting along southern Brazil and Namibia. Gondwana Research, 51, 170–176. https://doi.org/10.1016/j.gr.2017.08.001

Sawyer, S., Dale, M., F., C., Reston, J., Timothy, S., M., J., & Hopper, R. (2007). COBBOOM: The Continental Breakkup and Birth of Oceans Mission. Scientific Drilling, (5, Sept 2007). https://doi.org/10.2204/iodp.sd.5.02.2007

930   Schmitt, A. K., Emmermann, R., Trumbull, R. B., Bühn, B., & Henjes-Kunst, F. (2000). Petrogenesis and 40Ar/39Ar geochronology of the Brandberg complex, Namibia: Evidence for a major mantle contribution in metaluminous and peralkaline granites. Journal of Petrology, 41(8), 1207–1239. https://doi.org/10.1093/petrology/41.8.1207

Schwarz, G. (1978). Estimating the Dimension of a Model. The Annals of Statistics, 6(2), 461–464. https://doi.org/10.1214/aos/1176344136

935   Selway, K. (2014). On the Causes of Electrical Conductivity Anomalies in Tectonically Stable Lithosphere. Surveys in Geophysics, 35(1), 219–257. https://doi.org/10.1007/s10712-013-9235-1

Seton, M., Müller, R. D., Zahirovic, S., Gaina, C., Torsvik, T., Shephard, G., et al. (2012). Global continental and ocean basin reconstructions since 200Ma. Earth-Science Reviews, 113(3–4), 212–270. https://doi.org/10.1016/j.earscirev.2012.03.002

940   Stewart, J., Watts, A. B., & Bagguley, J. G. (2000). Three-dimensional subsidence analysis and gravity modelling of the continental margin offshore Namibia. Geophysical Journal International, 141(3), 724–746. https://doi.org/10.1046/j.1365-246x.2000.00124.x

Sun, J., & Li, Y. (2017). Joint inversion of multiple geophysical and petrophysical data using generalized fuzzy clustering algorithms. Geophysical Journal International, 208(2), 1201–1216. https://doi.org/10.1093/gji/ggw442

945   Teklay, M., Wirth, K., Mezger, K., & Thole, J. (2020). Picrites of the Jungfrau and Sargdeckel, central Namibia: Relative roles of mantle and crust in the Southern Etendeka large igneous province. Lithos, 354–355, 105283. https://doi.org/10.1016/j.lithos.2019.105283

Thompson, R. N., & Gibson, S. A. (1991). Subcontinental mantle plumes, hotspots and pre-existing thinspots. Journal of the Geological Society, 148(6), 973–977. https://doi.org/10.1144/gsjgs.148.6.0973

950   Torsvik, T. H., Rousse, S., Labails, C., & Smethurst, M. A. (2009). A new scheme for the opening of the South Atlantic Ocean and the dissection of an Aptian salt basin. Geophysical Journal International, 177(3), 1315–1333. https://doi.org/10.1111/j.1365-246X.2009.04137.x

Trumbull, R. B., Vietor, T., Hahne, K., Wackerle, R., & Ledru, P. (2004). Aeromagnetic mapping and reconnaissance geochemistry of the Early Cretaceous Henties Bay-Outjo dike swarm, Etendeka Igneous Province, Namibia. Journal of

955   African Earth Sciences, 40(1–2), 17–29. https://doi.org/10.1016/j.jafrearsci.2004.07.006

Weckmann, U., Ritter, O., & Haak, V. (2003). A magnetotelluric study of the Damara Belt in Namibia 2. MT phases over 90° reveal the internal structure of the Waterberg Fault/Omaruru Lineament. Physics of the Earth and Planetary Interiors, 138(2), 91–112. https://doi.org/10.1016/S0031-9201(03)00079-7

White, R. S., & McKenzie, D. (1989). Magmatism at rift zones: The generation of volcanic continental margins and flood

960   basalts. Journal of Geophysical Research, 94(B6), 7685. https://doi.org/10.1029/JB094iB06p07685

White, R. S., Spence, G. D., Fowler, S. R., McKenzie, D. P., Westbrook, G. K., & Bowen, A. N. (1987). Magmatism at rifted continental margins. Nature, 330(6147), 439–444. https://doi.org/10.1038/330439a0

Wilson, J. T. (1963). A possible origin of the Hawaiian Islands. Canadian Journal of Physics, 41(6), 863–870. https://doi.org/10.1139/p63-094

965   Worzewski, T., Jegen, M., & Swidinsky, A. (2012). Approximations for the 2-D coast effect on marine magnetotelluric data. Geophysical Journal International, 189(1), 357–368. https://doi.org/10.1111/j.1365-246X.2012.05385.x

Yuan, X., Heit, B., Brune, S., Steinberger, B., Geissler, W. H., Jokat, W., & Weber, M. (2017). Seismic structure of the lithosphere beneath NWNamibia: Impact of the Tristan da Cunha mantle plume. Geochemistry, Geophysics, Geosystems, 18(1), 125–141. https://doi.org/10.1002/2016GC006645

970   Zhao, D. (2007). Seismic images under 60 hotspots: Search for mantle plumes. Gondwana Research, 12(4), 335–355. https://doi.org/10.1016/j.gr.2007.03.001

Van Zijl, J. S. (1977). Electrical studies of the deep crust in various tectonic provinces of southern Africa. In The Earth's crust (Vol. 20, pp. 470–500). American Geophysical Union.